Estimation of Cutting Forces in Vibration Assisted Drilling System Using Augmented Kalman Filter

by

Kashif Nadeem
B.Eng, National University of Sciences and Technology (NUST), 2017

A thesis submitted in partial fulfillment of the requirements for the degree of
Master of Applied Science
in the Department of Mechanical Engineering

Estimation of Cutting Forces in Vibration Assisted Drilling System Using Augmented Kalman Filter

by

Kashif Nadeem
B.Eng, National University of Sciences and Technology (NUST), 2017

Supervisory Committee

Dr. Keivan Ahmadi, Supervisor
(Department of Mechanical Engineering)

Dr. Zuomin Dong, Departmental Member
(Department of Mechanical Engineering)

ABSTRACT

Vibration assisted drilling (VAD) is a type of machining process in which high-frequency vibrations with a small amplitude are induced in the cutting tool to improve the cutting process of hard and brittle materials. These vibrations create an unsteady repetitive processing effect which eventually reduce the cutting forces. It is also crucial to measure these forces in some way because their knowledge directly aids in determining the best machining parameters. Direct and indirect methods can be used to measure these forces, but due to serious limitations of direct measurement methods, an indirect measurement method is required which is capable of online monitoring of high-frequency cutting forces.

In this thesis, an indirect method is proposed to estimate thrust force and torque from the voltage signal generated by piezoelectric sensor and torsional deflection signal measured through piezoelectric accelerometer. The estimation of two input signals requires a multi-input multi-output (MIMO) model of VAD system which is developed using Receptance Coupling and Substructure Analysis (RCSA) method. Experimental and numerical methods are used to validate the constituent single-input single-output (SISO) transfer functions of the MIMO model. As the estimated forces are distorted by the dynamics of VAD structure, a Kalman Filter is employed to compensate the dynamics. The accuracy and similarity of results is determined by comparing the estimated cutting force values with the force measured from a load cell in time and frequency domain. The reported experimental results confirm the possibility of using Kalman Filter in estimating high-frequency forces generated in VAD process.

Contents

List of Tables

List of Figures

ACRONYMS

FRF Frequency Response Function

CM Conventional Machining

CD Conventional Drilling

VAM Vibration Assisted Machining

VAD Vibration Assisted Drilling

CFRP Carbon-Fibre-Reinforced Polymers

SISO Single-Input Single-Output

MIMO Multi-Input Multi-Output

RCSA Receptance Coupling Substructure Analysis

RD Regularized Deconvolution

AKF Augmented Kalman Filter

LTI Linear Time-Invariant

FEA Finite Element Analysis

DOF Degree of Freedom

LSCF Linear Square Complex Frequency Estimator

LSFD Least-Squares Frequency-Domain Estimator

FFT Fast Fourier Transform

ACKNOWLEDGEMENTS

It had been my long-standing goal to pursue a master's degree in Mechanical Engineering, and I am grateful to University of Victoria for providing me the opportunity to do so. Then I would want to express gratitude to my supervisor, Dr. Keivan Ahmadi, for his excellent mentoring and constructive criticism, which pushed me to improve as a research engineer. It was an honor to learn from his vast experience and knowledge. I would also like to thank my brother, Dr. Khurram Nadeem, who has always been a big supporter of mine and has helped me develop the essential aptitude which is necessary for higher studies.

I would like to thank all the members of DDM lab, especially Yaser and Vahid, for their invaluable consultation and advice. I also thank God for bringing me to the lovely Victoria, where I met so many friendly and like-minded people.

Finally I would like to thank all my family members for their unwavering support and for always allowing me to pursue my dreams.

Chapter 1

Introduction

Vibration-assisted machining (VAM) combines conventional machining (CM) and ultrasonic vibration. It is a rapidly developing technology aimed at increasing the productivity of machining processes. VAM is a processing method that uses a piezoelectric transducer for converting high-frequency electrical energy into high-frequency mechanical vibrations energy and applies it to the machining process, and achieves material removal by mechanical effect [9, 4]. A phenomenon of periodic intermittent processing occurs by applying high-frequency vibration [10, 21]. An illustration of VAM system is shown in Fig.1.1 in which a piezoelectric transducer (PZT) is configured into the tool to excite the tool in any desired direction. The tool oscillates at an ultrasonic frequency f (around 20 kHz) with a very small vibration amplitude a. The VAM is affected by vibration frequency f amplitude a and workpiece cutting speed v_c that determine the cutting force. According to theoretical studies, tool-workpiece contact ratio (TWCR) is a key factor in the VAM process. TWCR is defined as the percentage of time that the tool maintains contact with the workpiece, where the increase in both the tool vibration parameters (f and a) and decrease in cutting speed v_c reduce the TWCR which in turn reduces the cutting force.

Consequently, in comparison to conventional machining, the removal mechanism of materials is changed fundamentally because of the change in cutting characteristics [34, 31, 20]. Numerous experimental and theoretical investigations have considered VAM to be an effective method for processing hard-brittle materials such as nickel and titanium based super alloys, hardened steels, optical glasses, ceramics, tungsten carbides, etc. Compared to conventional machining, VAM not only improves the machining accuracy and efficiency of general workpiece materials, but also overcomes the

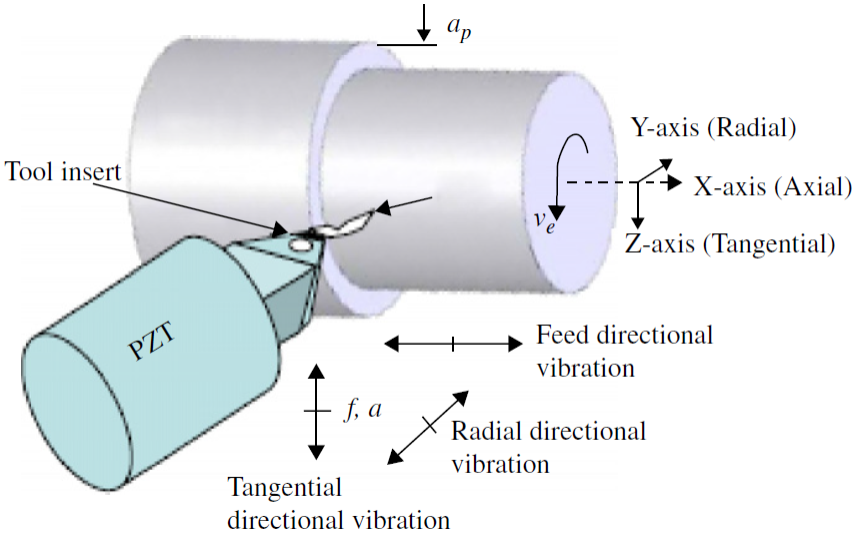

Figure 1.1: Schematic diagram of vibration assisted cutting [21]

problems of excessive cutting force, severe tool wear and subsurface defects caused by traditional machining processes [21, 35, 10].

Vibration-assisted drilling (VAD) is a type of VAM which offers numerous advantages such as extended tool life, reduced cutting force, cutting temperature, and improved machining quality. With VAD, drill life is increased four times as compared to conventional drilling (CD) methods [36]. It is also proved experimentally that with optimal processing conditions, the thrust force and torque are reduced by 20-30% [38]. In drilling composite materials, the delamination and fiber pullout is significantly decreased using VAD as compared to CD [30, 37].

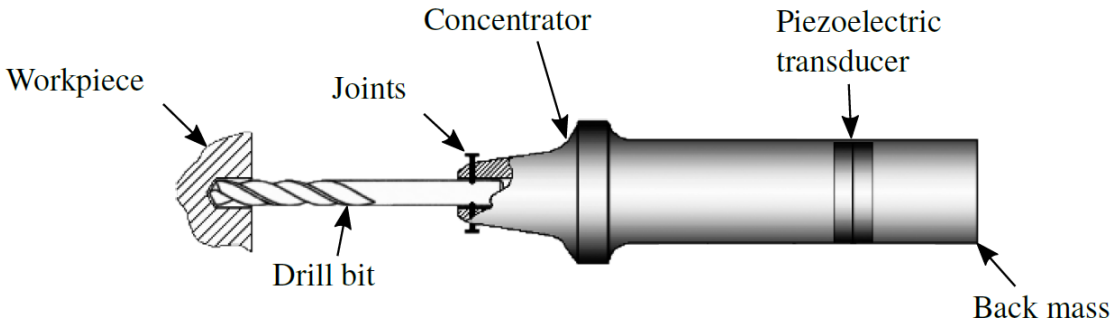

Figure 1.2: Components of a VAD tool holder [3]

Typical components of a VAD system are piezoelectric transducer, concentrator

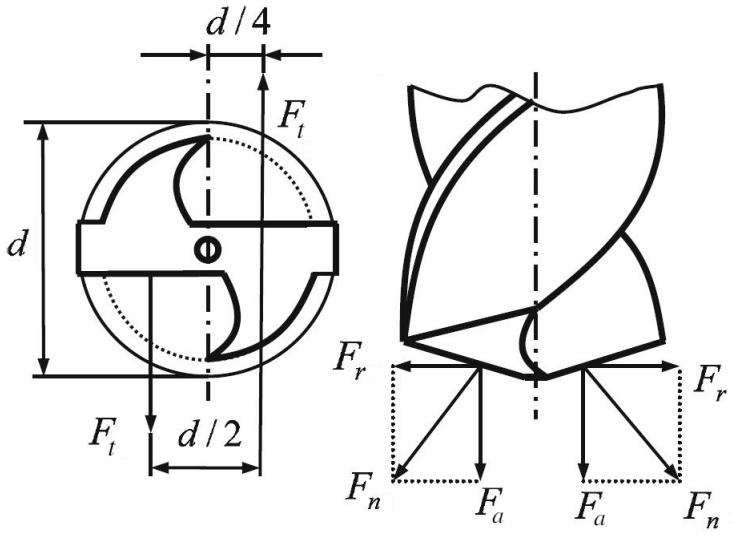

Figure 1.3: Components of cutting forces for drilling operation [7]

and a back mass as shown in Fig.1.2. Piezoelectric transducers generate vibrations when supplied with electric voltage. The amplitude of oscillation at the face of the transducer is too small to achieve any reasonable cutting rate therefore, the concentrator is used as an amplification device. For efficient machining to take place, the tool is designed with consideration given to mass and shape so that resonance can be achieved within frequency range capability of the ultrasonic machine. During drilling, chip removal forces consist of cutting force F_t, feed force (thrust force) F_a and radial force F_r whereas the torque T is the product of cutting force and diameter d of the drill bit as shown in Fig.1.3. The shape of the concentrator is designed in such a way that the vibrations are amplified at the tip of the drill bit in either single axial or in both axial-torsional directions. In case of axial concentrator, vibrations are induced in the feed direction but with axial-torsional concentrator part of vibrations are transformed into torsional motion, generating vibrations in both cutting and feed directions as shown in Fig.1.4 [39, 22].

The rear side of the tool holder is attached with a back mass which is cylindrical in shape. The purpose of the heavy back mass is to induce vibrations of high amplitude at the tip of the tool. So an optimally designed VAD tool holder concentrate high amplitude of vibrations at the tip of drill bit [19, 3].

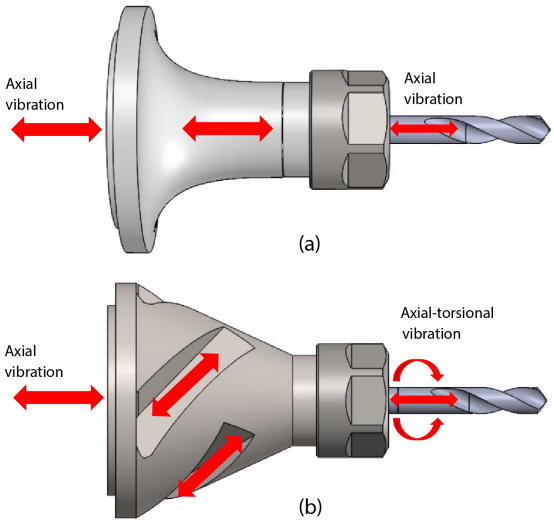

Figure 1.4: Propagation of axial vibration in (a) axial and (b) axial-torsional concentrator

1.1 Cutting force measurement

The importance of cutting force measurement and prediction is very crucial for process optimization in terms of tool performance, tool design, tool life, and optimal parameter determination [32]. Cutting forces are directly related to physics-based modeling of machining process, therefore they are most robust and accurate parameter for machining process monitoring. The estimation methods for determining the cutting force are classified into Direct estimation and Indirect estimation of the cutting force depending on the measurement used.

1.1.1 Direct measurement

Direct estimation of the cutting force involves measuring the cutting force directly from the tool-tip by utilizing external or internal sensors on the machine. Cutting forces can be measured directly using commercial table or rotating dynamometers as shown in Fig.1.5. Despite the accuracy and reliability of commercial dynamometers, their usage is limited due to high cost. Moreover, they suffer from limited workpiece sizes and mounting constraints. Altintas investigated the measurement of cutting forces in milling operation using Spindle-Integrated Force Sensors (SPIFS) mounted inside the stationary spindle housing. The SPIF sensors used in the study directly detect the cutting force by utilizing piezoelectric force sensor. As shown in Fig.1.6 the

Figure 1.5: (a) Table dynamometer; (b) Rotating dynamometer [16]

shear force in the X and Y axes is measured by two pairs of force sensors, while the force in Z-axis is measured by a pair of compression sensors. The authors achieve high accuracy by using Kalman Filter to eliminate disturbance generated by the system's structural dynamics [24].

In a study by Rizal, a rotating toolholder with an embedded strain gauge-based sensor is utilized to investigate the direct estimation approach. Similarly, Rizal studied the usage of a rotating tool with integrated multi-sensor system to measure the components of cutting force. In both of these studies, specifically designed rotating dynamometers are used to measure cutting forces. These investigations also indicate the possibility of measuring thermal effects and temperature variations in CNC system [27, 28].

1.1.2 Indirect estimation

Cutting force can also be determined by using some parameters available from CNC machine such as spindle motor current, voltage or vibrations [17]. It is observed that the variation of armature current in the feed drive motor depends on the load provided by the system [12].

Aslan proposed a method to determine the cutting forces from the armature current measured from the feed drive motor of five-axis milling machine. Cutting torque is calculated by subtracting the identified friction and inertia of each axis drive from the total torque of the servo motor. To remove the effect of disturbance caused by

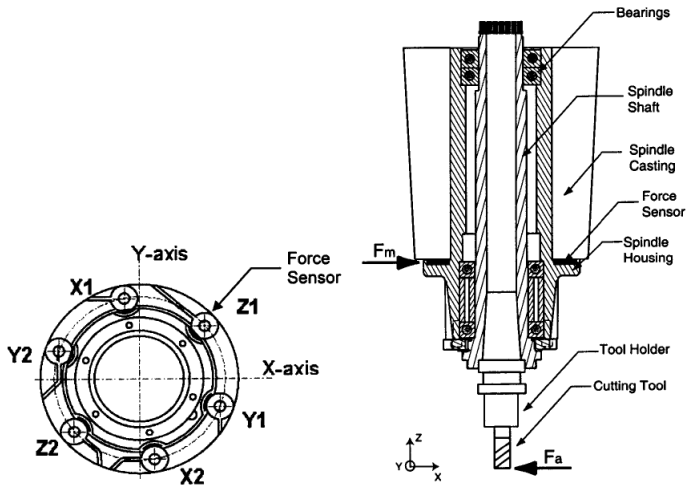

Figure 1.6: Sensor arrangement in dynamically compensated Spindle Integrated Force Sensor System [24]

structural modes of the machine, the author employs Kalman Filter, while the kinematics of the machine is modeled to get precise results [2].

In another study by Altintas, cutting force is determined by mounting accelerometers on the spindle housing [25]. This method is validated by conducting milling tests and using a dynamometer (Kistler 9265B). For a more accurate estimation, a Kalman filter is implemented to correct the cutting force values and enable the modeling of the proposed system.

For tool condition monitoring and indirect estimation of cutting forces, Albertelli employed external sensors. In his paper, an in-process model-based estimator was designed and tool-tip vibration were used to estimate the cutting forces. The author mounted a tri-axial accelerometer on spindle housing to measure acceleration and an inductive sensor to measure the relative radial displacement between spindle shaft and spindle housing. The observer used in the study relies on Kalman filter to estimate both cutting force and vibrations in the system. Furthermore, the usage of multiple sensors extend the frequency bandwidth of the estimated cutting force [1].

In another case of indirect measurement [33], cutting force is determined indirectly based on tool flank deflection. A displacement sensor is attached to the rotating tool shank to measure radial deflections. Then using the deflection and tool stiffness, which

is determined from substructure synthesis technique, cutting force is determined.

1.2 Research objective

The forces of interest in VAD are the ones which are induced by the piezoelectric actuator and the external forces involved in the cutting of carbon-fibre-reinforced polymers (CFRP). Although the cutting forces can be measured directly by using commercial dynamometer but the forces involved in VAD are of high frequency so therefore exceed the bandwidth of the dynamometer, which is a major limitation in the application of dynamometer to the measurement of high frequency forces. Their usage is also limited due to high cost and difficulty in incorporating them into the machine tool system without compromising the system dynamics. To solve this problem, a nonintrusive measurement method is required to do the online monitoring of high frequency dynamic cutting forces. So the indirect force estimation method proposed in this study will enable proactive monitoring of cutting forces without using bulky dynamometers. As a result, the knowledge of these forces will allow to select the optimal machining parameters and also ensure process monitoring.

The availability of piezoelectric disks in VAD provides us a great opportunity to estimate forces without using external sensors. However the piezoelectric disks are located away from the tool tip so the measured forces are the convolution of structural dynamics of the tool and the cutting forces. The deconvolution of forces from the structural dynamics is an ill-posed problem and the results obtained are often unstable. Also in the estimation of both thrust force and torque, a multi-input-multi-output (MIMO) model is required to consider the influence of cross-talk between inputs and outputs. Since in VAD process, toolholder is excited near its high-frequency resonance modes which are in the range of 15 kHz to 22 kHz, therefore conventional experimental modal analysis techniques such as impact hammer and shaker test are incapable of exciting the required high frequencies. In order to overcome this problem, the constituent single-input single-output (SISO) FRFs of complex MIMO model are developed using Receptance Coupling and Substructure Analysis (RCSA) method. With this approach FRFs are theoretically calculated in any desired frequency range. So this research aims to develop a low-cost and non-intrusive indirect measurement method by using voltage signal from the embedded piezoelectric sensor and the torsional deflection from an externally attached piezoelectric accelerometer. The distur-

bance effect of the VAD structure is compensated by designing a state-observer based on Augmented Kalman Filter (AKF) method.

1.3 Thesis organization

The rest of the thesis is organized in the following manner: In Chapter 2, two methods for inverse force estimation are discussed first followed by receptance coupling method RCSA and theoretical expressions to model individual components. In Chapter 3, two main subassemblies of VAD system are coupled to obtain single-input single-output (SISO) FRFs. Then after the validation of SISO models, system identification is performed to obtain multi-input multi-output (MIMO) state-space model. In Chapter 4, Augmentand Kalman Filter (AKF) method is implemented besides the presentation of a series of experimental test results. Chapter 5 gives the conclusions.

Chapter 2

Background Theory

2.1 Inverse force reconstruction

A linear time-invariant (LTI) system with n-state variables, p-input and q-output in discrete time can be described by a system of equations

$$\{x(k+1)\} = [A]\{x(k)\} + [B]u(k) \tag{2.1}$$

$$y(k) = [C]\{x(k)\} \tag{2.2}$$

where $x(k)$ are states of the system, $u(k)$ is the input signal, $y(k)$ is the output signal, $[A]$ is state transition matrix, $[B]$ is input distribution matrix and $[C]$ is output distribution matrix. The two set of equations are called n^{th} order state-space equations. Eq.2.1 consists of a set of n first-order matrix differential equations, whereas Eq.2.2 is made up of q algebraic equations. The output signal $y(k)$ of LTI system can also be represented as the convolution sum of input signal $u(k)$ and the impulse response of the system [14]

$$y(k) = \sum_{\tau=0}^{k} g(\tau)u(k-\tau) = g(k) * u(k) \tag{2.3}$$

where $g(\tau)$ is the impulse response function of the system and $*$ is the convolution product. The impulse response function is expressed in terms of the system matrices as follows:

$$g(\tau) = 0 \quad \text{for} \quad \tau \leq 0, \quad \text{and} \quad g(\tau) = [C]\,[A]^{\tau-1}\,[B] \quad \text{for} \quad \tau = 1, 2, \ldots \tag{2.4}$$

Discretization of the convolution integral yields a matrix equation.

$$[y(k)] = [G][u(k)] \tag{2.5}$$

where $[G]$ is the transfer matrix. With the knowledge of matrix $[G]$ or the availability of a system model in the form of state equations, inverse problem deals with the prediction of system input $u(k)$ from the physical measurement of system output $y(k)$. However it is an established fact that the matrix $[G]$ is ill-conditioned and therefore the deconvolution (inverse problem) of the system defined by Eq.2.5 leads to unstable solutions that fluctuate even further with minor disturbances such as noise [11]. In case of state equations, simple state observers produce erroneous and delayed results corrupted by disturbances and sensor noise.

In the following sections, two methods are presented which deal with the ill-posedness of inverse problem by employing regularization and by formulating the problem while taking disturbances into consideration. Although in this work Augmented Kalman Filter (AKF) is considered as the main method to estimate input forces, the Regularized Deconvolution (RD) is also described. RD is not considered in the estimation of cutting forces because it is an offline method and can not be applied to online force estimation.

2.1.1 Regularized deconvolution (RD)

The matrix equation, which maps the input signal $u(k)$ to the corresponding output measured response $y(k)$ through the transfer matrix, is obtained by repeating Eq.2.3 for N successive timesteps as [14].

$$\begin{bmatrix} y(0) & y(1) & \cdots & y(N-1) \end{bmatrix}^T = [G] \begin{bmatrix} u(0) & u(1) & \cdots & u(N-1) \end{bmatrix}^T \tag{2.6}$$

where the transfer matrix $[G]$ is given as

$$[G] = \begin{bmatrix} g(0) & 0 & \cdots & 0 \\ g(1) & g(0) & \cdots & 0 \\ \vdots & \vdots & \vdots & \vdots \\ g(N-1) & g(N-2) & \cdots & g(0) \end{bmatrix} \tag{2.7}$$

Using the output response signal $\{y(k); k = 0..N-1\}$, input signal $\{u(k); k =$

$0..N-1\}$ can be estimated from the inverse solution of Eq.2.6. However, matrix $[G]$ is ill-conditioned so to address the ill-posedness of problem, a regularization factor α is introduced into the inverse solution of Eq.2.6 to balance the estimation error and noise magnification.

$$\begin{Bmatrix} \hat{u}(0) \\ \hat{u}(1) \\ \vdots \\ \hat{u}(N-1) \end{Bmatrix} = \begin{bmatrix} G \\ \sqrt{\alpha} I_{N\times N} \end{bmatrix}^{+} \begin{Bmatrix} y(0) \\ y(1) \\ \vdots \\ y(N-1) \\ 0_{N\times N} \end{Bmatrix} \tag{2.8}$$

where $^{+}$ represents Moore Penrose inverse, while $\hat{}$ denotes the estimated input signal.

2.1.2 Augmented kalman filter (AKF)

VAD system is embedded with two piezoelectric transducer disks, in which one of them is used as an actuator and the other one as a sensor. The AKF method will be used to reconstruct the thrust force and torque which are being applied at the tip of drill bit using the voltage signal from the piezoelectric sensor and torsional displacement signal from the piezoelectric accelerometer.

AKF method essentially consists of standard Kalman Filter [15] being applied to the augmented state-space model. The dynamics of a system with n-state variables, p-input and q-output is formulated into the discrete-time state space form as

$$\begin{aligned} \{x(k+1)\} &= [A]\{x(k)\} + [B]u(k) + \{w(k)\} \\ y(k) &= [C]\{x(k)\} \end{aligned} \tag{2.9}$$

where *w(k)* is component of process noise associated with state vector $\{x(k)\} \in \mathbb{R}^n$, $[A] \in \mathbb{R}^{n\times n}$ is the system matrix and $[B] \in \mathbb{R}^{n\times p}$ and $[C] \in \mathbb{R}^{q\times n}$ are corresponding input and output distribution matrices respectively. The input vector is assumed to be constant with $\eta(k)$ as the stochastic component of the process given by

$$u(k+1) = u(k) + \eta(k) \tag{2.10}$$

Eq.2.10 allows the estimation of input signal time history through appropriate

choice of the covariance matrix $[S]$ of the process $\eta(k)$. This covariance matrix will be used to regularize the inverse estimation problem by using a method explained in Section 4.4. In AKF method, the unknown input signals are treated as additional states with constant stochastic dynamics. Applying this assumption to the state space model in Eq.2.9 converts it to the following augmented state space model that simultaneously describes the dynamics of the system as well as the input signal variations:

$$\{x_a(k+1)\} = [A_a]\{x_a(k)\} + \{\zeta(k)\} \tag{2.11}$$

where the augmented states, system matrices and process noise vector are as follows

$$\{x_a(k)\} = \begin{Bmatrix} x(k) \\ u(k) \end{Bmatrix}; [A_a] = \begin{bmatrix} A & B \\ 0_{p\times n} & I_p \end{bmatrix}; \{\zeta(k)\} = \begin{Bmatrix} \omega(k) \\ \eta(k) \end{Bmatrix}; [C_a] = \begin{bmatrix} C & 0_{q\times q} \end{bmatrix} \tag{2.12}$$

Subsequently, the measurement vector is also expressed in terms of the augmented state as

$$y(k) = [C_a]\{x_a(k)\} + v(k) \tag{2.13}$$

here $[C_a]$ is the augmented measurement matrix and *v(k)* represents the measurement noise. The process noise *w(k)*, component of stochastic process $\eta(k)$ and measurement noise *v(k)* are assumed to be white with covariance matrices $[Q] \in \mathbb{R}^{n\times n}$, $[R]$ and $[S]$ respectively. The covariance matrices $[R]$ and $[S]$ are scalar with diagonal values given as

$$[R] = \begin{bmatrix} R_v & 0 \\ 0 & R_\theta \end{bmatrix}; [S] = \begin{bmatrix} S_f & 0 \\ 0 & S_t \end{bmatrix} \tag{2.14}$$

where R_v is covariance of sensor voltage signal V^2, R_θ is covariance of accelerometer signal $(\frac{m}{s^2})^2$, S_f is regularization factor for force N^2 and S_t is regularization factor for torque $(N.m)^2$. The value of estimated augmented state $\hat{x}_a(k)$ is obtained from the measurements of *y(k)* using the following Kalman Filter observer which recursively update the estimation of augmented states of Eq.2.11

$$\begin{aligned} \{\hat{x}_a(k)\}^- &= [A_a]\{\hat{x}_a(k-1)\}^+ \\ \{\hat{x}_a(k)\}^+ &= \{\hat{x}_a(k)\}^- + \{L(k)\}\left(\mathrm{y}(k) - [C_a]\{\hat{x}_a(k)\}^-\right) \end{aligned} \tag{2.15}$$

where - and + superscripts indicate a priori and posteriori estimations respectively, whereas $\left(\mathrm{y}(k) - [C_a]\{\hat{x}_a(k)\}^-\right)$ is the innovation term. At each time step Kalman gain *L(k)* is computed as [5]

$$\{L(k)\} = [P(k)]^- [C_a]^T [SS(k)]^{-1} \tag{2.16}$$

here *[SS(k)]* is the innovation covariance which is given by

$$[SS(k)] = [C_a][P(k)]^- [C_a]^T + R \tag{2.17}$$

whereas the covariance matrix *[P(k)]* of state estimation error is calculated as

$$[P(k)]^- = [A_a][P(k-1)]^+ [A_a]^T + [\bar{Q}]; [\bar{Q}] = \begin{bmatrix} Q & 0_{n\times p} \\ 0_{p\times n} & S \end{bmatrix} \tag{2.18}$$

here $[\bar{Q}]$ is augmented covariance matrix. The state estimation error is updated for the next step of the iteration as

$$[P(k)]^+ = [P(k)]^- - \{L(k)\}[C_a][P(k)]^- \tag{2.19}$$

In the steady state, the kalman gain of linear time-invariant (LTI) system in Eq.2.15 converges to a constant value $\{L_\infty\}$, converting the Kalman observer to a Luenberger's state observer [5] described by the following state-space model:

$$\begin{aligned} \{\hat{x}_a(k)\}^+ &= ([A_a] - \{L_\infty\}[C_a][A_a])\{\hat{x}_a(k-1)\}^+ + \{L_\infty\}y(k) \\ \hat{y}(k) &= \left[\bar{C}_a\right]\{\hat{x}_a(k)\}^+ \end{aligned} \tag{2.20}$$

where $\left[\bar{C}_a\right] = [0_{p\times n}, I_p]$.

2.2 Receptance coupling substrucure analysis

As presented in the previous section that the AKF is applied to the state space model of the system. The system matrices $\{A, B, C\}$ of the state space model can be realized from its transfer matrix given as $G(s) = C(sI - A)^{-1}B$. This transfer matrix can be obtained from the transfer functions which describes the relation-

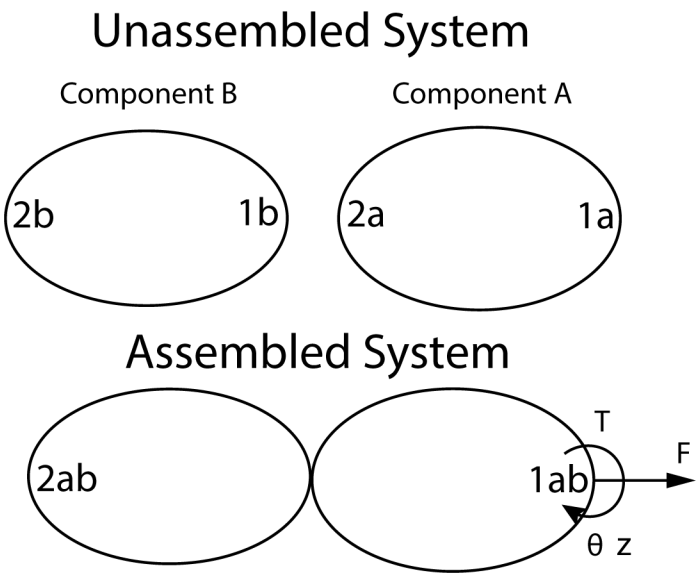

Figure 2.1: Rigid coupling of two components

ship between the input and output of the system. So the objective is to find the single-input-single-output (SISO) transfer functions using receptance coupling and substructural analysis. These individual transfer functions are used to develop the multi-input-multi-output (MIMO) transfer matrix of the VAD system which is then used to realize the system matrices to form state equations.

Receptance coupling enables the prediction of frequency response function (FRF) of an assembly using the FRF of its subsystems. The Frequency Response Functions (FRFs) of subsystems can be obtained using different techniques. One of the few modelling options to compute FRF of individual components include continuous system theory and finite element solutions. The FRFs can also be acquired using experimental measurements.

Consider Fig.2.1 in which two components with free-free boundry conditions are coupled rigidly. The receptance matrices of the two components A and B can be written as

$$[H_A] = \begin{bmatrix} [h_{1a1a}] & [h_{1a2a}] \\ [h_{2a1a}] & [h_{2a2a}] \end{bmatrix} \tag{2.21}$$

$$[H_B] = \begin{bmatrix} [h_{1b1b}] & [h_{1b2b}] \\ [h_{2b1b}] & [h_{2b2b}] \end{bmatrix} \tag{2.22}$$

Note that all the displacements, forces and receptance matrices are functions of frequency which is not represented in the equations for simplicity. The submatrices in equations 2.21 and 2.22 contain the end point direct and cross transfer receptance functions of each component:

$$\begin{aligned} [h_{1a1a}] &= \begin{bmatrix} \frac{z_{1a}}{f_{1a}} & \frac{z_{1a}}{t_{1a}} \\ \frac{\theta_{1a}}{f_{1a}} & \frac{\theta_{1a}}{t_{1a}} \end{bmatrix} \quad [h_{1a2a}] = \begin{bmatrix} \frac{z_{1a}}{f_{2a}} & \frac{z_{1a}}{t_{2a}} \\ \frac{\theta_{1a}}{f_{2a}} & \frac{\theta_{1a}}{t_{2a}} \end{bmatrix} \\ [h_{2a1a}] &= \begin{bmatrix} \frac{z_{2a}}{f_{1a}} & \frac{z_{2a}}{t_{1a}} \\ \frac{\theta_{2a}}{f_{1a}} & \frac{\theta_{2a}}{t_{1a}} \end{bmatrix} \quad [h_{2a2a}] = \begin{bmatrix} \frac{z_{2a}}{f_{2a}} & \frac{z_{2a}}{t_{2a}} \\ \frac{\theta_{2a}}{f_{2a}} & \frac{\theta_{2a}}{t_{2a}} \end{bmatrix} \end{aligned} \tag{2.23}$$

and

$$\begin{aligned} [h_{1b1b}] &= \begin{bmatrix} \frac{z_{1b}}{f_{1b}} & \frac{z_{1b}}{t_{1b}} \\ \frac{\theta_{1b}}{f_{1b}} & \frac{\theta_{1b}}{t_{1b}} \end{bmatrix} \quad [h_{1b2b}] = \begin{bmatrix} \frac{z_{1b}}{f_{2b}} & \frac{z_{1b}}{t_{2b}} \\ \frac{\theta_{1b}}{f_2} & \frac{\theta_{1b}}{t_{2b}} \end{bmatrix} \\ [h_{2b1b}] &= \begin{bmatrix} \frac{z_{2b}}{f_{1b}} & \frac{z_{2b}}{t_{1b}} \\ \frac{\theta_{2b}}{f_{1b}} & \frac{\theta_{2b}}{t_{1b}} \end{bmatrix} \quad [h_{2b2b}] = \begin{bmatrix} \frac{z_{2b}}{f_{2b}} & \frac{z_{2b}}{t_{2b}} \\ \frac{\theta_{2b}}{f_{2b}} & \frac{\theta_{2b}}{t_{2b}} \end{bmatrix} \end{aligned} \tag{2.24}$$

The submatrix receptance functions in equations 2.21 and 2.22 give the following relations:

$$\begin{Bmatrix} z_i \\ \theta_i \end{Bmatrix} = \begin{bmatrix} h_{ij}^{zf} & h_{ij}^{zt} \\ h_{ij}^{\theta f} & h_{ij}^{\theta t} \end{bmatrix} \begin{Bmatrix} f_j \\ t_j \end{Bmatrix} \tag{2.25}$$

In Eq.2.25, z represents axial displacement and θ torsional displacement at DOF i, where $i = 1a$, $2a$, $1b$ and $2b$ whereas f represents axial force and t torque applied at DOF j, where $j = 1a$, $2a$, $1b$ and $2b$. The following equations can be written for component A:

$$\begin{Bmatrix} z_{1a} \\ \theta_{1a} \end{Bmatrix} = [h_{1a1a}] \begin{Bmatrix} f_{1a} \\ t_{1a} \end{Bmatrix} + [h_{1a2a}] \begin{Bmatrix} f_{2a} \\ t_{2a} \end{Bmatrix} \tag{2.26}$$

$$\begin{Bmatrix} z_{2a} \\ \theta_{2a} \end{Bmatrix} = [h_{2a1a}] \begin{Bmatrix} f_{1a} \\ t_{1a} \end{Bmatrix} + [h_{2a2a}] \begin{Bmatrix} f_{2a} \\ t_{2a} \end{Bmatrix} \tag{2.27}$$

and similarly, for component B, we have

$$\left\{ \begin{array}{c} z_{1b} \\ \theta_{1b} \end{array} \right\} = [h_{1b1b}] \left\{ \begin{array}{c} f_{1b} \\ t_{1b} \end{array} \right\} + [h_{1b2b}] \left\{ \begin{array}{c} f_{2b} \\ t_{2b} \end{array} \right\} \tag{2.28}$$

$$\left\{ \begin{array}{c} z_{2b} \\ \theta_{2b} \end{array} \right\} = [h_{2b1b}] \left\{ \begin{array}{c} f_{1b} \\ t_{1b} \end{array} \right\} + [h_{2b2b}] \left\{ \begin{array}{c} f_{2b} \\ t_{2b} \end{array} \right\} \tag{2.29}$$

The compatibilty condition at the coordinates $1b$ and $2a$ is defined by the displacement vectors as

$$\left\{ \begin{array}{c} z_{1b} \\ \theta_{1b} \end{array} \right\} = \left\{ \begin{array}{c} z_{2a} \\ \theta_{2a} \end{array} \right\} \tag{2.30}$$

Equilibrium condition which relates the internal forces of two components at the coupling point is defined as

$$\left\{ \begin{array}{c} f_{1b} \\ t_{1b} \end{array} \right\} = - \left\{ \begin{array}{c} f_{2a} \\ t_{2a} \end{array} \right\} \tag{2.31}$$

The substitution of equations 2.27 and 2.28 in the compatibility Eq.2.30 gives,

$$[h_{1b1b}] \left\{ \begin{array}{c} f_{1b} \\ t_{1b} \end{array} \right\} + [h_{1b2b}] \left\{ \begin{array}{c} f_{2b} \\ t_{2b} \end{array} \right\} = [h_{2a1a}] \left\{ \begin{array}{c} f_{1a} \\ t_{1a} \end{array} \right\} + [h_{2a2a}] \left\{ \begin{array}{c} f_{2a} \\ t_{2a} \end{array} \right\} \tag{2.32}$$

Employing equilibrium Eq.2.31 in Eq.2.32 and rearranging for force and torque at coordinate $2a$ yield

$$\left\{ \begin{array}{c} f_{2a} \\ t_{2a} \end{array} \right\} = \left([h_{2a2a}] + [h_{1b1b}] \right)^{-1} [h_{1b2b}] \left\{ \begin{array}{c} f_{2b} \\ t_{2b} \end{array} \right\} - \left([h_{2a2a}] + [h_{1b1b}] \right)^{-1} [h_{2a1a}] \left\{ \begin{array}{c} f_{1a} \\ t_{1a} \end{array} \right\} \tag{2.33}$$

Then using Eq.2.33 in Eq.2.26 gives the relation as

$$\begin{aligned} \left\{ \begin{array}{c} z_{1a} \\ \theta_{1a} \end{array} \right\} = & \left([h_{1a1a}] - [h_{1a2a}] \left([h_{2a2a}] + [h_{1b1b}] \right)^{-1} [h_{2a1a}] \right) \left\{ \begin{array}{c} f_{1a} \\ t_{1a} \end{array} \right\} + \\ & \left([h_{1a2a}] \left([h_{2a2a}] + [h_{1b1b}] \right)^{-1} [h_{1b2b}] \right) \left\{ \begin{array}{c} f_{2b} \\ t_{2b} \end{array} \right\} \end{aligned} \tag{2.34}$$

Since the assembly coordinates $2ab$ and $1ab$ are located at the same physical location as $2b$ and $1b$ respectively

$$\left\{ \begin{array}{c} z_{1ab} \\ \theta_{1ab} \end{array} \right\} = \left\{ \begin{array}{c} z_{1a} \\ \theta_{1a} \end{array} \right\}; \left\{ \begin{array}{c} z_{2ab} \\ \theta_{2ab} \end{array} \right\} = \left\{ \begin{array}{c} z_{2b} \\ \theta_{2b} \end{array} \right\} \tag{2.35}$$

$$\left\{ \begin{array}{c} f_{1ab} \\ t_{1ab} \end{array} \right\} = \left\{ \begin{array}{c} f_{1a} \\ t_{1a} \end{array} \right\}; \left\{ \begin{array}{c} f_{2ab} \\ t_{2ab} \end{array} \right\} = \left\{ \begin{array}{c} f_{2b} \\ t_{2b} \end{array} \right\} \tag{2.36}$$

therefore,

$$\begin{aligned} \left\{ \begin{array}{c} z_{1ab} \\ \theta_{1ab} \end{array} \right\} = & \left([h_{1a1a}] - [h_{1a2a}] \left([h_{2a2a}] + [h_{1b1b}] \right)^{-1} [h_{2a1a}] \right) \left\{ \begin{array}{c} f_{1ab} \\ t_{1ab} \end{array} \right\} + \\ & \left([h_{1a2a}] \left([h_{2a2a}] + [h_{1b1b}] \right)^{-1} [h_{1b2b}] \right) \left\{ \begin{array}{c} f_{2ab} \\ t_{2ab} \end{array} \right\} \end{aligned} \tag{2.37}$$

which gives the two direct and cross FRF matrices as follows

$$[h_{1ab1ab}] = [h_{1a1a}] - [h_{1a2a}] \left([h_{2a2a}] + [h_{1b1b}] \right)^{-1} [h_{2a1a}] \tag{2.38}$$

$$[h_{1ab2ab}] = [h_{1a2a}] \left([h_{2a2a}] + [h_{1b1b}] \right)^{-1} [h_{1b2b}] \tag{2.39}$$

For the remaining two FRFs, rewriting the Eq.2.33 and by using the equilibrium condition of Eq.2.31, we have

$$\left\{ \begin{array}{c} f_{1b} \\ t_{1b} \end{array} \right\} = - \left([h_{2a2a}] + [h_{1b1b}] \right)^{-1} [h_{1b2b}] \left\{ \begin{array}{c} f_{2b} \\ t_{2b} \end{array} \right\} + \left([h_{2a2a}] + [h_{1b1b}] \right)^{-1} [h_{2a1a}] \left\{ \begin{array}{c} f_{1a} \\ t_{1a} \end{array} \right\} \tag{2.40}$$

this relation is then used in Eq.2.29 to give

$$\begin{aligned} \left\{ \begin{array}{c} z_{2b} \\ \theta_{2b} \end{array} \right\} = & \left([h_{2b1b}] \left([h_{2a2a}] + [h_{1b1b}] \right)^{-1} [h_{2a1a}] \right) \left\{ \begin{array}{c} f_{1a} \\ t_{1a} \end{array} \right\} + \\ & \left([h_{2b2b}] - [h_{2b1b}] \left([h_{2a2a}] + [h_{1b1b}] \right)^{-1} [h_{1b2b}] \right) \left\{ \begin{array}{c} f_{2b} \\ t_{2b} \end{array} \right\} \end{aligned} \tag{2.41}$$

Now once again using the equations 2.35 and 2.36 and rewriting Eq.2.41

$$\left\{ \begin{array}{c} z_{2ab} \\ \theta_{2ab} \end{array} \right\} = \left([h_{2b1b}] \left([h_{2a2a}] + [h_{1b1b}] \right)^{-1} [h_{2a1a}] \right) \left\{ \begin{array}{c} f_{1ab} \\ t_{1ab} \end{array} \right\} + \left([h_{2b2b}] - [h_{2b1b}] \left([h_{2a2a}] + [h_{1b1b}] \right)^{-1} [h_{1b2b}] \right) \left\{ \begin{array}{c} f_{2ab} \\ t_{2ab} \end{array} \right\} \tag{2.42}$$

So the remaining two direct and cross FRF of the assembled system are computed as

$$[h_{2ab1ab}] = [h_{2b1b}] \left([h_{2a2a}] + [h_{1b1b}] \right)^{-1} [h_{2a1a}] \tag{2.43}$$

$$[h_{2ab2ab}] = [h_{2b2b}] - [h_{2b1b}] \left([h_{2a2a}] + [h_{1b1b}] \right)^{-1} [h_{1b2b}] \tag{2.44}$$

Equations 2.38, 2.39, 2.43 and 2.44 provide the direct and cross receptances of assembly which are written as a function of the substructure receptances and the final FRF matrix of the assembled system is formed as

$$[H_{AB}] = \left[\begin{array}{cc} [h_{1ab1ab}] & [h_{1ab2ab}] \\ [h_{2ab1ab}] & [h_{2ab2ab}] \end{array} \right] \tag{2.45}$$

2.3 Receptance modelling of subcomponents

As mentioned earlier that the substructure receptance matrices can be generated by measurements, continuous system theory and finite element solutions. The analytical and numerical approach used to model subcomponents is discussed in the following sections.

2.3.1 Receptance modelling of cylindrical rod

The displacement and torsional deformation to force and torque receptances of uniform cylindrical components could be represented by closed form expressions [22]. For a simple free-free cylindrical shaped flexible rod with coordinates i and and j specified at each end, the direct and cross axial FRFs is given by:

$$h_{ij}^{zf}(z_i, z_j, \omega) = \frac{z_i}{f_j} = \sum_{n=0}^{N_m} \frac{U_n(z_i) U_n(z_j)}{-\omega^2 + \omega_n^2} \tag{2.46}$$

where ω_n is the natural frequency of n^{th} mode N_m whereas U_0 and U_n represent the rigid body and mass-normalized axial mode shapes of the corresponding mode respectively, obtained as follows [26]:

$$\omega_n = \frac{n\pi}{l}\sqrt{\frac{E}{\rho}}; U_0(z) = \frac{1}{\sqrt{\rho A l}}; U_n(z) = \sqrt{\frac{2}{\rho A l}}\cos\frac{n\pi z}{l} \tag{2.47}$$

here $n = 0, 1, 2, ...,$ and z is the distance from the free end of the rod. E is the elastic modulus, l is the length of rod, ρ is density and A is the cross-section area of the rod. Now for the same elastic rod, the direct and cross torsional FRF between coordinates i and j is synthesized as

$$h_{ij}^{\theta t}(z_i, z_j, \omega) = \frac{\theta_i}{t_j} = \sum_{n=0}^{N_m} \frac{\Theta_n(z_i)\,\Theta_n(z_j)}{-\omega^2 + \omega_n^2} \tag{2.48}$$

where ω_n is the natural frequency of n^{th} mode N_m whereas Θ_0 and Θ_n represent the rigid body and mass-normalized torsional mode shapes of the corresponding mode respectively, obtained as follows

$$\omega_n = \frac{n\pi}{l}\sqrt{\frac{G}{\rho}}; \Theta_0(z) = \frac{1}{\sqrt{\rho J l}}; \Theta_n(z) = \sqrt{\frac{2}{\rho J l}}\cos\frac{n\pi z}{l} \tag{2.49}$$

where G is modulus of rigidity and J is polar moment of inertia. So the receptance matrix containing both the axial and torsional FRFs at two ends of rod component will be obtained as follows

$$H_r = \begin{bmatrix} H_{1r1r} & H_{1r2r} \\ H_{2r1r} & H_{2r2r} \end{bmatrix} = \begin{bmatrix} h_{1r1r}^{zf}(0,0,\omega) & 0 & h_{1r2r}^{zf}(0,l,\omega) & 0 \\ 0 & h_{1r1r}^{\theta t}(0,0,\omega) & 0 & h_{1r2r}^{\theta t}(0,l,\omega) \\ h_{2r1r}^{zf}(l,0,\omega) & 0 & h_{2r2r}^{zf}(l,l,\omega) & 0 \\ 0 & h_{2r1r}^{\theta t}(l,0,\omega) & 0 & h_{2r2r}^{\theta t}(l,l,\omega) \end{bmatrix} \tag{2.50}$$

2.3.2 Coupled axial-torsional finite element modelling of pre-twisted geometry

In case of a pre-twisted geometry, the axial and torsional deflections are coupled. It can be seen in Fig.2.2 that when this element is subjected with either axial force f

or torque t, both Δz axial and $\Delta\theta$ torsional deflections are produced simultaneously.

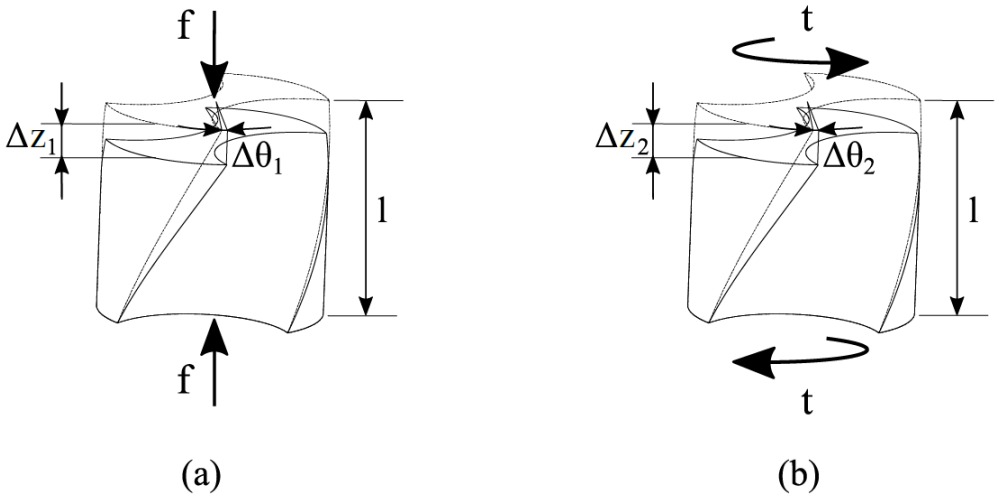

Figure 2.2: Deformations of twisted geometry under a) an axial force b) a torsional torque[22]

The relationship between force and torque inducing axial and torsional deflection is described by a non-linear model [29].

$$f = EA\varepsilon + ES\varphi + \frac{1}{2}EI_p\varphi^2 \tag{2.51}$$

$$t = ES\varepsilon + (GJ_s + EK)\,\varphi + EI_p\varepsilon\varphi + \frac{3}{2}ED\varphi^2 + \frac{1}{2}EF\varphi^3 \tag{2.52}$$

where ε is axial strain, φ is change in torsional displacement per unit length, E is modulus of elasticity, G is modulus of rigidity, A is cross section area, I_p is polar moment of inertia whereas S, J_s, K, D and F are for section integral parameters which depend on geometrical dimensions of the cross-section [29]. The effect of non-linear terms in equations 2.51 and 2.52 are less than 1% of the linear terms [13]. Therefore, the effect of non-linearities are neglected and the twisted-element is approximated as a linear axial-torsional spring described by following equations.

$$f = k^{zf}\Delta z + k^{\theta f}\Delta\theta \tag{2.53}$$

$$t = k^{zt}\Delta z + k^{\theta t}\Delta\theta \tag{2.54}$$

where the stiffness coefficients are expressed as follows:

$$k^{zf} = \frac{EA}{l}; k^{\theta f} = \frac{ES}{l}; k^{zt} = \frac{ES}{l}; k^{\theta t} = \frac{(GJ_s + EK_s)}{l} \tag{2.55}$$

The values of stiffness coefficients used in this work were determined by a curve-fitting method [22]. First a pre-twisted rod element was modelled in a commercial FEA software (COMSOL Multiphysics) then considering two cases, force and torque was applied separately. The resultant deformations and known force and torque were used in equations 2.53 and 2.54 to form four simultaneous equations. Finally after solving these equations, stiffness coefficients k^{zf}, $k^{\theta f}$, k^{zt} and $k^{\theta t}$ were determined. The stiffness and mass matrix were obtained for Tungsten Carbide material of unit length l and modulus of elasticity E_{wc}, expressed as follows [22]:

$$[k] = \frac{E}{lE_{WC}} \begin{bmatrix} k^{zf} & k^{\theta f} & -k^{zf} & -k^{\theta f} \\ k^{zt} & k^{\theta t} & -k^{zt} & -k^{\theta t} \\ -k^{zf} & -k^{\theta f} & k^{zf} & k^{\theta f} \\ -k^{zt} & -k^{\theta t} & k^{zt} & k^{\theta t} \end{bmatrix} \tag{2.56}$$

$$[m] = \begin{bmatrix} \frac{m}{3} & 0 & \frac{m}{6} & 0 \\ 0 & \frac{I}{3} & 0 & \frac{I}{6} \\ \frac{m}{6} & 0 & \frac{m}{3} & 0 \\ 0 & \frac{I}{6} & 0 & \frac{I}{3} \end{bmatrix} \tag{2.57}$$

where m is mass and I is moment of inertia. Elemental description of equations 2.56 and 2.57 is applied to all the elements of the body which leads to the formation of global stiffness matrix $[K]$ and global mass matrix $[M]$. These system matrices are then converted into eigenvalue matrix Λ and eigenvector matrix Φ.

$$[\Lambda] = \begin{bmatrix} \omega_1^2 & 0 & \dots & 0 \\ 0 & \omega_2^2 & \dots & 0 \\ \vdots & \vdots & \ddots & \vdots \\ 0 & 0 & \dots & \omega_{(2N_e+2)}^2 \end{bmatrix} \tag{2.58}$$

$$[\Phi] = \begin{bmatrix} \{\phi_1\} & \{\phi_2\} & \cdots & \{\phi_{(2N_e+2)}\} \end{bmatrix} \tag{2.59}$$

where N_e is the number of elements. Using natural frequencies and mode shapes from equations 2.58 and 2.59, the FRF of the body is computed from the following equation.

$$h_{jk}(\omega) = \sum_{r=1}^{2N_e+2} \frac{\phi_{jr}\phi_{jr}}{\omega_r^2 + \omega^2} \tag{2.60}$$

here j refers to the coordinates of axial displacement z and torsional displacement θ whereas k represents the coordinates of axial force f and torque t. The FRF matrix of the overall system is formulated as

$$H_s = \begin{bmatrix} H_{1s1s} & H_{1s2s} \\ H_{2s1s} & H_{2s2s} \end{bmatrix} = \begin{bmatrix} h_{1,1}(\omega) & h_{1,2}(\omega) & h_{1,(2N_e+1)}(\omega) & h_{1,(2N_e+2)}(\omega) \\ h_{2,1}(\omega) & h_{2,2}(\omega) & h_{2,(2N_e+1)}(\omega) & h_{2,(2N_e+2)}(\omega) \\ h_{(2N_e+1),1}(\omega) & h_{(2N_e+1),2}(\omega) & h_{(2N_e+1),(2N_e+1)}(\omega) & h_{(2N_e+1),(2N_e+2)}(\omega) \\ h_{(2N_e+2),1}(\omega) & h_{(2N_e+2),2}(\omega) & h_{(2N_e+2),(2N_e+1)}(\omega) & h_{(2N_e+2),(2N_e+2)}(\omega) \end{bmatrix} \tag{2.61}$$

Chapter 3

Modelling VAD System Dynamics

3.1 Multi input multi output system

Dynamics of an assembled system is determined by the interaction of the dynamics of its individual components. In this chapter, Receptance Coupling and Substructure Analysis (RCSA) is used to combine the dynamic models of VAD components to determine the response of sensors to all the inputs. The single-input-single-output (SISO) transfer functions obtained from RCSA are used to form the multi-input-multi-output (MIMO) transfer matrix. From the MIMO transfer matrix, the system matrices $\{A, B, C\}$ will be realized and used in the Augmented Kalman Filter algorithm to estimate the input forces.

The VAD toolholder consist of tightening bolt, back mass, piezoelectric transducer, concentrator and a drill bit, which are assembled in series. Table 3.1 lists the material properties associated with each component, whereas the drawing of each component is provided in Appendix A.

Table 3.1: Material properties of VAD components

	Drill bit	Piezoelectric	Other
Density (kg/m^3)	15,630	7600	7800
Young's modulus (GPa)	530	63	200
Poisson's ratio (1)	0.3	-	0.3
Piezoelectric constant (m/V or C/N)	-	300×10^{-12}	-

The assembly of the components form a subsystem mbp which consist of bolt, back-mass and piezoelectric transducer and another subsystem cd which consist of concentrator and the drill bit as shown in Fig.3.1. The inputs to the VAD system are the external force F and torque T applied at the degree of freedom $2cd$ and the actuation voltage V_a applied at the piezoelectric actuator defined by DOFs $1mbp$ and $2mbp$. The outputs are the voltage signal V_s obtained from piezoelectric sensor and the torsional deflection θ measured using piezoelectric accelerometer at the degree of freedom $1cd$.

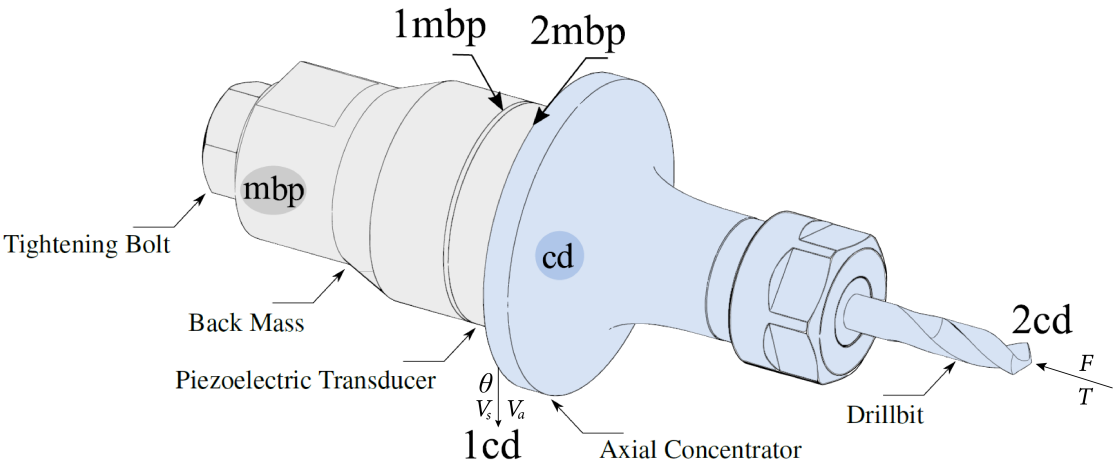

Figure 3.1: Components of VAD tool holder [23]

The input-output relationship of VAD system can be written in the state-space representation with n-state variables, 3-inputs and 2-outputs as follows:

$$\begin{aligned} x(k+1) &= [A]x(k) + [B]\begin{Bmatrix} F(k) \\ T(k) \\ V_a(k) \end{Bmatrix} \\ \begin{Bmatrix} V_s(k) \\ \theta(k) \end{Bmatrix} &= [C]x(k) \end{aligned} \tag{3.1}$$

where $[A]$, $[B]$ and $[C]$ are system matrices. The state-space formulation given in Eq.3.1 can be turned into transfer function matrix $[G]$ as

$$G(s) = C(sI - A)^{-1}B \tag{3.2}$$

where $[G]$ is 2×3 transfer function matrix which is a collection of six single-input single-output (SISO) transfer functions that maps each input with each output in frequency domain as

$$\begin{Bmatrix} V_s(\omega) \\ \theta(\omega) \end{Bmatrix} = \begin{bmatrix} G(\omega) \end{bmatrix} \begin{Bmatrix} F(\omega) \\ T(\omega) \\ V_a(\omega) \end{Bmatrix} \tag{3.3}$$

or

$$\begin{Bmatrix} V_s(\omega) \\ \theta(\omega) \end{Bmatrix} = \begin{bmatrix} h_{VsF} & h_{VsT} & h_{V_sV_a} \\ h_{\theta F} & h_{\theta T} & h_{\theta V_a} \end{bmatrix} \begin{Bmatrix} F(\omega) \\ T(\omega) \\ V_a(\omega) \end{Bmatrix} \tag{3.4}$$

In the following sections, the six single-input-single-output transfer functions are obtained using Receptance Coupling and Substructure Analysis (RCSA).

3.2 Finding single-input single-output FRF using RCSA

To theoretically characterize the electromechanical response of vibration assisted drilling system to the input signals, the SISO Frequency Response Function (FRF) between each input and output variable is computed using Receptance Coupling Substructure analysis (RCSA). In this approach, RCSA method is used to mathematically assemble the Frequency Response Functions (FRFs) of the individual components to obtain the response at the sensors when input signals are applied to the VAD system. Based on the geometry of components, analytical or simplified finite element models are used to obtain the FRFs of individual components. The detailed derivations of the coupling of each component is not presented in this work and can be found in Ostad Ali Akbari, Vahid's thesis [22]. The stiffness and damping at the drill-concentrator and concentrator-piezoelectric interfaces is also considered by modelling them as linear springs and dampers as shown in Fig.3.2.

In the following sections only the last step of coupling is presented in which the bolt, backmass and piezo subassembly (mbp) is coupled with the concentrator and drill bit subassembly (cd).

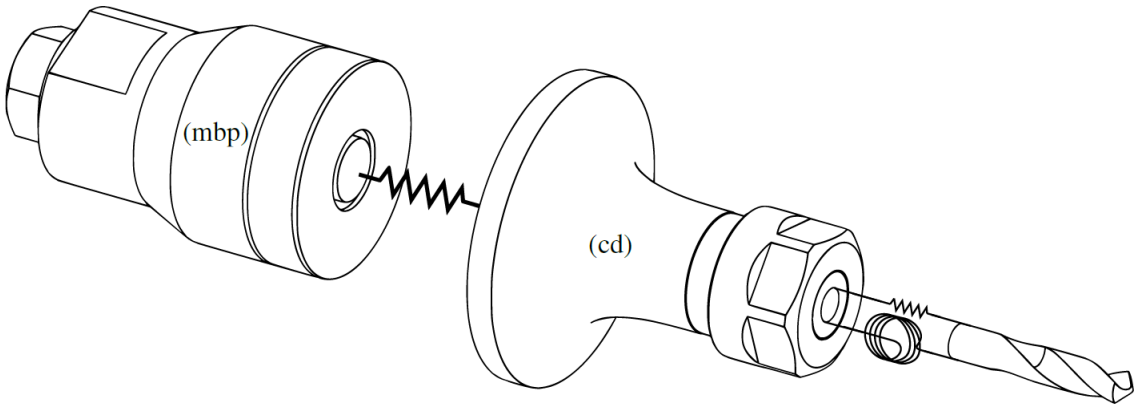

Figure 3.2: RCSA model with joint stiffness and damping [22]

3.2.1 Transfer function between sensor voltage and input force and torque

Here the objective is to determine the FRF between the sensor voltage V_s generated due to axial deformation at the degree of freedom $1mbp$ and $2mbp$ of piezoelectric transducer and the high frequency force and torque applied at the degree of freedom $2cd$ as shown in Fig.3.3. The displacement and force vectors respectively are defined as $\{X\} = [z, \theta]^T$ and $\{F_{\text{ext}}\} = [F, T]^T$. Compatibility conditions governing the coupling of mbp and cd subassemblies are expressed as $X_{2mbp} = X_{1cd}$ whereas the equilibrium conditions are $F_{2cd} = F_{\text{ext}}$ and $F_{2mbp} + F_{1cd} = 0$.

The component displacements for mbp subassembly at two degrees of freedom $1mbp$ and $2mbp$ are given by Eqn.3.5 and Eqn.3.6

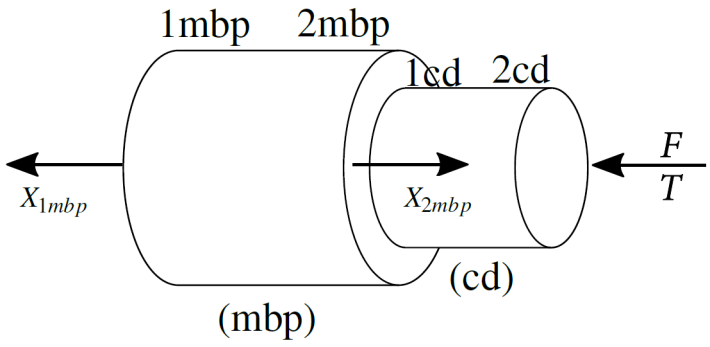

Figure 3.3: Schematic coupling model of subsystems for computation of FRF between sensor voltage and cutting forces [22]

$$X_{1mbp} = H_{1mbp1mbp}F_{1mbp} + H_{1mbp2mbp}F_{2mbp} \tag{3.5}$$

$$X_{2mbp} = H_{2mbp2mbp}F_{2mbp} + H_{2mbp1mbp}F_{1mbp} \tag{3.6}$$

here X_{1mbp} and X_{2mbp} represent the displacements at the two ends of the piezoelectric disk as shown in Fig. 3.1. The component displacements for *cd* subassembly at two degrees of freedom $1cd$ and $2cd$ are given by Eqn.3.7 and Eqn.3.8

$$X_{1cd} = H_{1cd1cd}F_{1cd} + H_{1cd2cd}F_{2cd} \tag{3.7}$$

$$X_{2cd} = H_{2cd2cd}F_{2cd} + H_{2cd1cd}F_{1cd} \tag{3.8}$$

Substituting for the displacements in the compatibility equation and using the equilibrium conditions F_{1cd} = - F_{2mbp} and F_{2cd}= F_{ext} with the elimination of F_{1mbp} = 0 gives Eqn.3.9

$$\begin{gathered} X_{2mbp} - X_{1cd} = H_{2mbp2mbp}F_{2mbp} - H_{1cd1cd}F_{1cd} - H_{1cd2cd}F_{2cd} = 0 \\ H_{2mbp2mbp}F_{2mbp} + H_{1cd1cd}F_{2mbp} - H_{1cd2cd}F_{\text{ext}} = 0 \\ F_{2mbp}\left(H_{2mbp2mbp} + H_{1cd1cd}\right) = H_{1cd2cd}F_{\text{ext}} \\ F_{2mbp} = \left(H_{2mbp2mbp} + H_{1cd1cd}\right)^{-1} H_{1cd2cd}F_{\text{ext}} \\ \text{or} \\ F_{1cd} = -\left(H_{2mbp2mbp} + H_{1cd1cd}\right)^{-1} H_{1cd2cd}F_{\text{ext}} \end{gathered} \tag{3.9}$$

The axial deformation of the piezoelectric sensor caused by mechanical forces is the difference between two degrees of freedom:

$$\begin{gathered} X_{1mbp} - X_{2mbp} = H_{1mbp2mbp}F_{2mbp} - H_{2mbp2mbp}F_{2mbp} \\ X_{1mbp} - X_{2mbp} = F_{2mbp}\left(H_{1mbp2mbp} - H_{2mbp2mbp}\right) \\ X_{1mbp} - X_{2mbp} = \left(H_{2mbp2mbp} + H_{1cd1cd}\right)^{-1} H_{1cd2cd}F_{\text{ext}}\left(H_{1mbp2mbp} - H_{2mbp2mbp}\right) \end{gathered} \tag{3.10}$$

The overall deflection of the piezoelectric element is related to the sensor voltage V_s as:

$$X_{1mbp} - X_{2mbp} = \frac{V_s C l S^E}{d_{im} A} \tag{3.11}$$

where C is the capacitance of the piezoelectric material, A is the cross-section area, l is the thickness of the disk, S^E is compliance coefficient ($\frac{m^2}{N}$) and d_{im} is the strain constant ($\frac{m}{V}$). Finally, the substitution of Eqn.3.11 into Eqn.3.10 yields the expression of FRF function with the measured voltage as output and external force as the input to the system. This relation is given in Eqn.3.12 as:

$$\begin{aligned}
&\left(H_{2mbp2mbp} + H_{1cd1cd}\right)^{-1} H_{1cd2cd} F_{ext} \left(H_{1mbp2mbp} - H_{2mbp2mbp}\right) = \frac{V_s C l S^E}{d_{im} A} \\
&\frac{V_s}{F_{\text{ext}}} = \frac{d_{im} A}{V_s C l S^E} \left\{\left(H_{2mbp2mbp} + H_{1cd1cd}\right)^{-1} H_{1cd2cd} \left(H_{1mbp2mbp} - H_{2mbp2mbp}\right)\right\}
\end{aligned} \tag{3.12}$$

Note that cross receptances for excitation at degree of freedom $2cd$, and measurement at mbp are expressed as:

$$\begin{bmatrix} h^{zF}_{mbp2cd} & h^{zT}_{mbp2cd} \\ h^{\theta F}_{mbp2cd} & h^{\theta T}_{mbp2cd} \end{bmatrix} = \left(H_{2mbp2mbp} + H_{1cd1cd}\right)^{-1} H_{1cd2cd} \left(H_{1mbp2mbp} - H_{2mbp2mbp}\right) \tag{3.13}$$

therefore, the FRF between sensor voltage V_s and axial force F is given as

$$\frac{V_s}{F} = \frac{d_{im} A}{V_s C l S^E} h^{zF}_{mbp2cd} \tag{3.14}$$

whereas, the FRF between sensor voltage V_s and torque T is given as

$$\frac{V_s}{T} = \frac{d_{im} A}{V_s C l S^E} h^{zT}_{mbp2cd} \tag{3.15}$$

Fig.3.4 shows the resultant FRF obtained using equations 3.14 and 3.15.

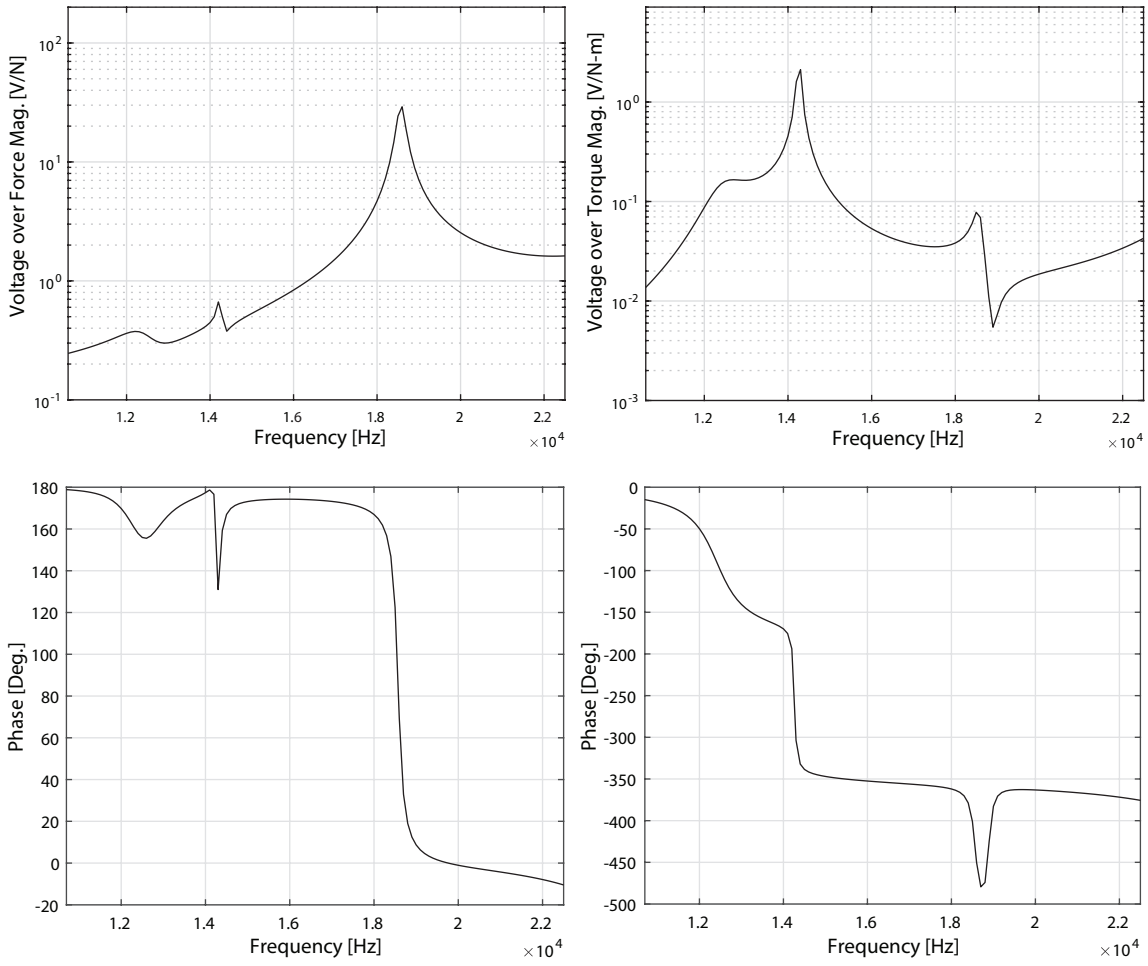

Figure 3.4: FRF between sensor voltage and input force and torque

3.2.2 Transfer function between torsional deformation and input force and torque

The computation of FRFs between the torsional deformation θ produced at the degree of freedom $1cd$ and the force and torque applied at the degree of freedom $2cd$ as shown in Fig.3.5, is presented in this section. The displacement and force vectors respectively are defined as $\{X\} = [z, \theta]^T$ and $\{F_{\text{ext}}\} = [F, T]^T$. Compatibility conditions governing the coupling of mbp and cd subassemblies are expressed as $X_{2mbp} = X_{1cd}$ whereas, the equilibrium conditions are $F_{2cd} = F_{\text{ext}}$ and $F_{2mbp} + F_{1cd} = 0$. The component displacements for mbp subassembly at two degrees of freedom $1mbp$ and $2mbp$ are given by Eqn.3.16 and Eqn.3.17

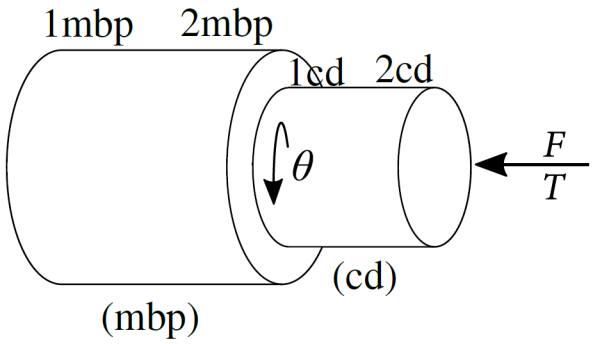

Figure 3.5: Schematic coupling model of subsystems for computation of FRF between torsional deflection and cutting forces [22]

$$X_{1mbp} = H_{1mbp1mbp}F_{1mbp} + H_{1mbp2mbp}F_{2mbp} \tag{3.16}$$

$$X_{2mbp} = H_{2mbp2mbp}F_{2mbp} + H_{2mbp1mbp}F_{1mbp} \tag{3.17}$$

The component displacements for cd subassembly at two degrees of freedom $1cd$ and $2cd$ are given by Eqn.3.18 and Eqn.3.19

$$X_{1cd} = H_{1cd1cd}F_{1cd} + H_{1cd2cd}F_{2cd} \tag{3.18}$$

$$X_{2cd} = H_{2cd2cd}F_{2cd} + H_{2cd1cd}F_{1cd} \tag{3.19}$$

Substituting for the displacements in the compatibility equation and using the equilibrium conditions F_{1cd} = - F_{2mbp} and F_{2cd}= F_{ext} with the elimination of F_{1mbp} = 0 gives Eqn.3.20

$$F_{1cd} = -\left(H_{2mbp2mbp} + H_{1cd1cd}\right)^{-1} H_{1cd2cd}F_{\text{ext}} \tag{3.20}$$

Using Eqn.3.20, the cross receptance matrix, mapping the displacement at DOF $1cd$ to the force vector at DOF $2cd$ is defined as

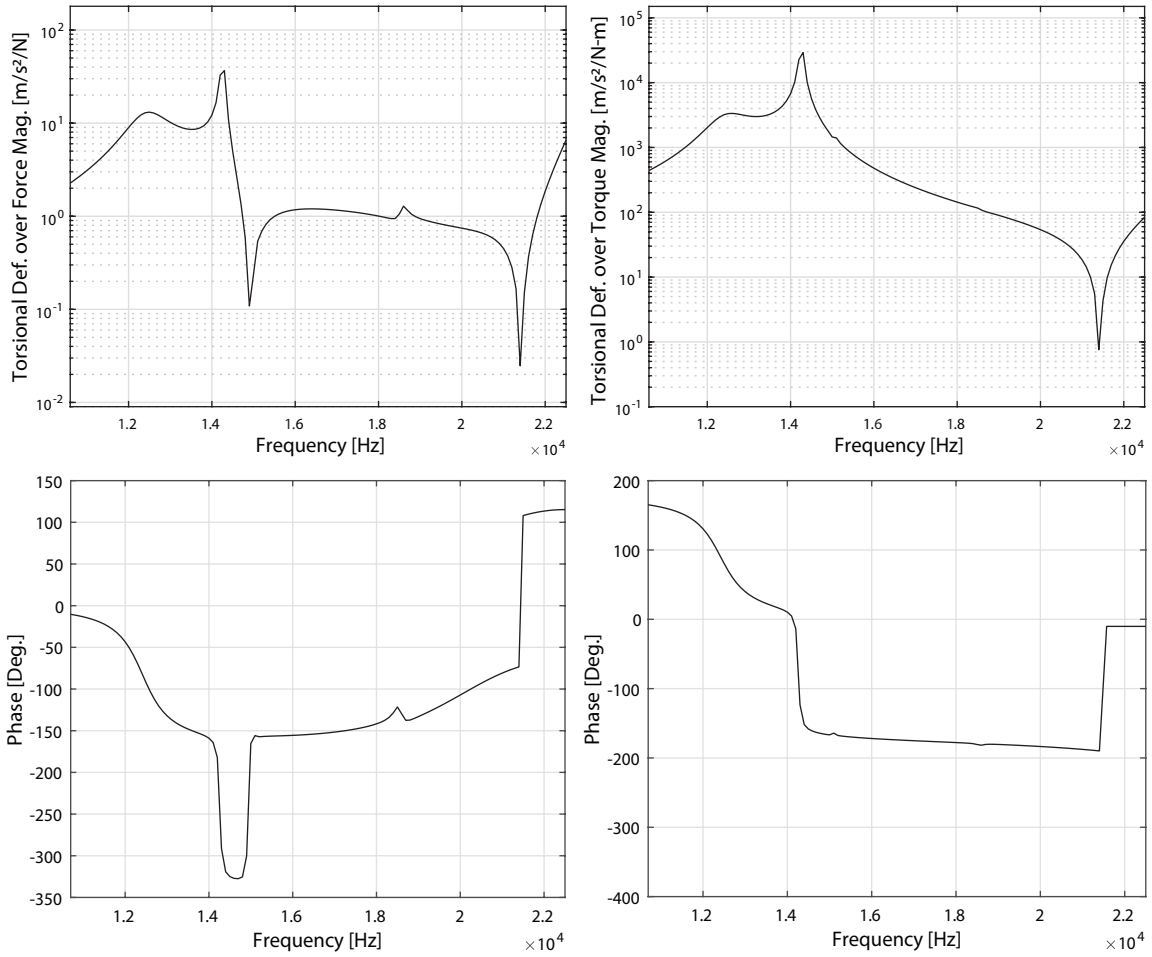

Figure 3.6: FRF between torsional deformation and input force and torque

$$\begin{aligned}
&\begin{bmatrix} h^{zF}_{1cd2cd} & h^{zT}_{1cd2cd} \\ h^{\theta F}_{1cd2cd} & h^{\theta T}_{1cd2cd} \end{bmatrix} = \frac{X_{1cd}}{F_{\text{ext},2cd}} = \frac{H_{1cd1cd}F_{1cd} + H_{1cd2cd}F_{\text{ext}}}{F_{\text{ext}}} \\
&\rightarrow \frac{X_{1cd}}{F_{\text{ext},2cd}} = \frac{H_{1cd2cd}F_{\text{ext}} - H_{1cd1cd}\left(H_{2mbp2mbp} + H_{1cd1cd}\right)^{-1} H_{1cd2cd}F_{\text{ext}}}{F_{\text{ext}}} \\
&\frac{X_{1cd}}{F_{\text{ext},2cd}} = H_{1cd2cd} - H_{1cd1cd}\left(H_{2mbp2mbp} + H_{1cd1cd}\right)^{-1} H_{1cd2cd}
\end{aligned} \tag{3.21}$$

so the FRF between torsional deflection θ and force F is given by

$$\frac{\theta_{1cd}}{F_{2cd}} = h^{\theta F}_{1cd2cd} \tag{3.22}$$

and the FRF between torsional deflection θ and torque T is given as

$$\frac{\theta_{1cd}}{T_{2cd}} = h^{\theta T}_{1cd2cd} \tag{3.23}$$

Note that the output signal from accelerometer is in $(\frac{m}{sec^2})$, therefore unit conversion for $h^{\theta F}_{1cd2cd}$ and $h^{\theta T}_{1cd2cd}$ is performed as:

$$h^{\theta F}_{1cd2cd}\left[\frac{m/sec^2}{N}\right] = r_c\left\{h^{\theta F}_{1cd2cd}\left[\frac{rad}{N}\right]\right\}\omega^2, h^{\theta T}_{1cd2cd}\left[\frac{m/sec^2}{N.m}\right] = r_c\left\{h^{\theta T}_{1cd2cd}\left[\frac{rad}{N.m}\right]\right\}\omega^2 \tag{3.24}$$

where r_c is the radius of the concentrator at piezo-concentrator joint. Fig.3.6 shows the resultant FRFs obtained using equations 3.22 and 3.23.

3.2.3 Transfer function between torsional deformation and actuation voltage

The computation of FRF between torsional deformation θ and actuation voltage V_a is presented in this section. The effect of voltage applied to the piezoelectric transducer is represented by the pair of opposite-direction forces F_{a} as shown in Fig.3.7

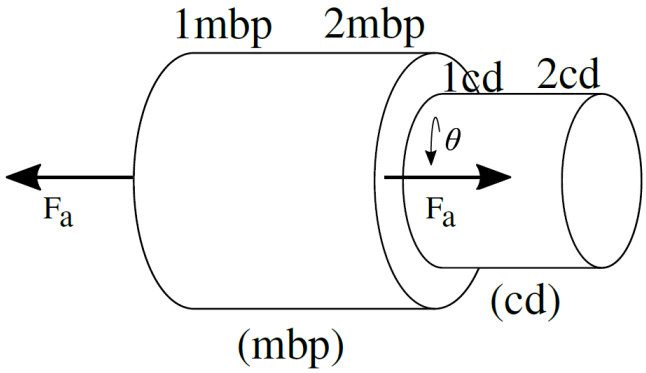

Figure 3.7: Effect of actuation voltage as a pair of forces at piezoelectric disk [22]

The compatibility condition is as follow

$$X_{2mbp} = X_{1cd} \tag{3.25}$$

The following relations hold for equilibrium condition of the forces

$$\begin{aligned} F_{1mbp} &= F_{\mathrm{a}} \\ F_{2mbp} + F_{1cd} &= -F_{\mathrm{a}} \end{aligned} \tag{3.26}$$

The DOF $1pcd$ is the focal point of this formulation. Considering the subsystem cd, the displacement vector $1cd$ is computed through the following equation

$$X_{1cd} = H_{1cd1cd} F_{1cd} \tag{3.27}$$

In Eqn.3.27 the force vector F_{1cd} should be replaced as a function of F_{a}. Using the compatibility condition from Eqn.3.25

$$\begin{aligned}
X_{2mbp} = X_{1cd} &\rightarrow H_{2mbp1mbp} F_{1mbp} + H_{2mbp2mbp} F_{2mbp} = H_{1cd1cd} F_{1cd} \\
&\rightarrow H_{2mbp1mbp} F_{\mathrm{a}} + H_{2mbp2mbp} \left(-F_{1cd} - F_{\mathrm{a}}\right) = H_{1cd1cd} F_{1cd} \\
&H_{2mbp1mbp} F_{\mathrm{a}} - H_{2mbp2mbp} F_{1cd} - H_{2mbp2mbp} F_{\mathrm{a}} = H_{1cd1cd} F_{1cd} \\
&F_{1cd} \left(H_{1cd1cd} + H_{2mbp2mbp}\right) = F_{\mathrm{a}} \left(H_{2mbp1mbp} - H_{2mbp2mbp}\right) \\
&F_{1cd} = \left(H_{1cd1cd} + H_{2mbp2mbp}\right)^{-1} \left(H_{2mbp1mbp} - H_{2mbp2mbp}\right) F_{\mathrm{a}}
\end{aligned} \tag{3.28}$$

Substituting F_{1cd} from Eqn.3.28 into Eqn.3.27,

$$\begin{aligned}
&X_{1cd} = H_{1cd1cd} \left(H_{1cd1cd} + H_{2mbp2mbp}\right)^{-1} \left(H_{2mbp1mbp} - H_{2mbp2mbp}\right) F_{\mathrm{a}} \\
\rightarrow &\begin{bmatrix} h^{zF}_{1cdmbp} & h^{zT}_{1cdmbp} \\ h^{\theta F}_{1cdmbp} & h^{\theta T}_{1cdmbp} \end{bmatrix} = H_{1cd1cd} \left(H_{1cd1cd} + H_{2mbp2mbp}\right)^{-1} \left(H_{2mbp1mbp} - H_{2mbp2mbp}\right)
\end{aligned} \tag{3.29}$$

here unit conversion for $h^{\theta F}_{1cdmbp}$ is performed as:

$$h^{\theta F}_{1cdmbp} \left[\frac{m/sec^2}{N}\right] = r_c \left\{ h^{\theta F}_{1cdmbp} \left[\frac{rad}{N}\right] \right\} \omega^2 \tag{3.30}$$

The relation between F_{a} and actuation voltage V_a is given by the equation [22].

$$F_{\mathrm{a}} = \left\{ \ \frac{Ad}{8} \left(\rho l \omega^2 - \frac{\pi^2}{l S^E}\right) V_a \ \right\} \tag{3.31}$$

where A is the cross-section area, d is the strain constant ($\frac{m}{V}$), ρ is piezoelectric density, l is the thickness of the disk and S^E is compliance coefficient ($\frac{m^2}{N}$). So the final relation which relates the torsional deformation at DOF $1cd$ to the excitation voltage V_a at DOF mbp is written as

$$\frac{\theta_{1cd}}{V_{a,mbp}} = \frac{Ad}{8} \left(\rho l \omega^2 - \frac{\pi^2}{l S^E}\right) h^{\theta F}_{1cdmbp} \tag{3.32}$$

Fig.3.8 shows the resultant FRF obtained using Eqn.3.32

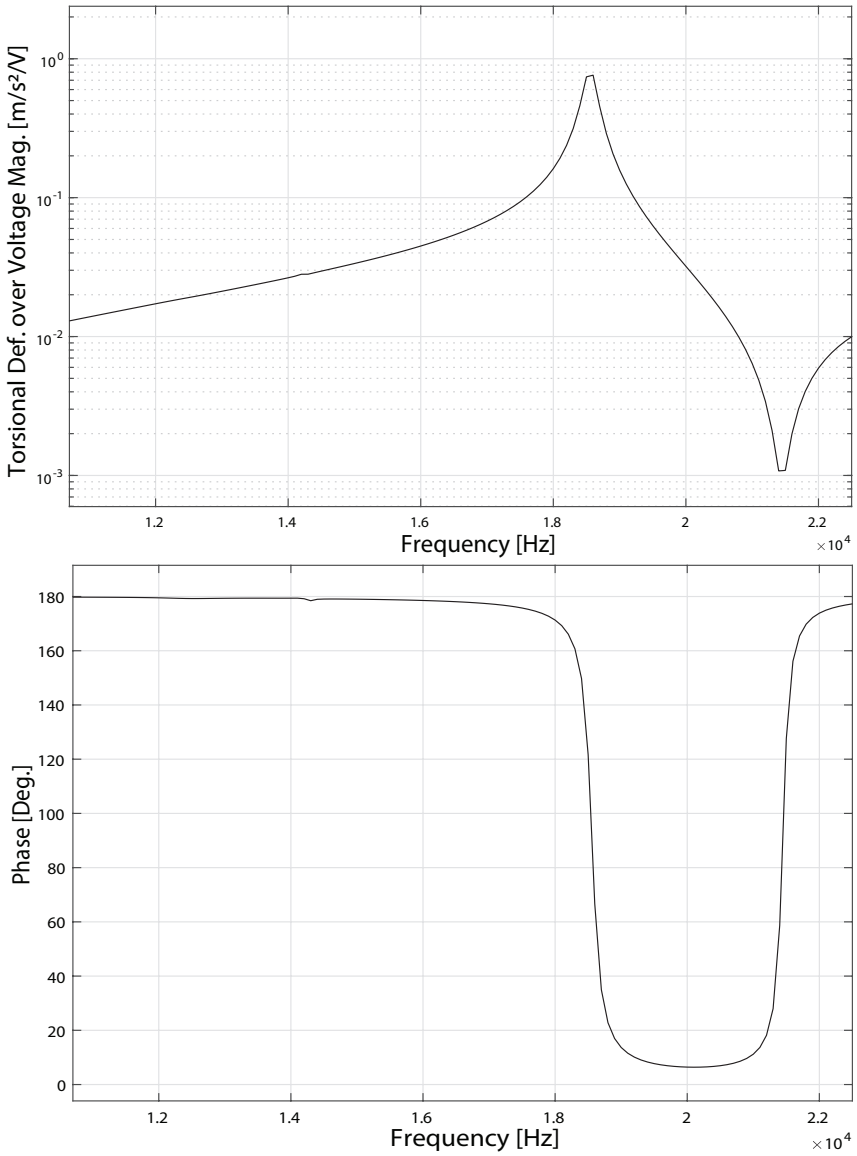

Figure 3.8: FRF between torsional deformation and actuation voltage

3.2.4 Transfer function between sensor voltage and actuation voltage

The computation of FRF between sensor voltage V_s and actuation voltage V_a is presented in this section. Since VAD is embedded with two piezoelectric transducer disks, therefore in this case the actuator disk is joined with backmass-bolt to form

subassembly *mbp* and the sensor disk is joined with the concentrator-drill to from subassembly *pcd* as shown in Fig.3.9. The effect of voltage applied to the piezoelectric transducer is represented by the pair of opposite-direction forces F_{a}, whereas the joint of sensor disk with concentrator-drill assembly is at the DOF $2cd'$. The displacement vector is defined as $\{X\} = [z, \theta]^T$.

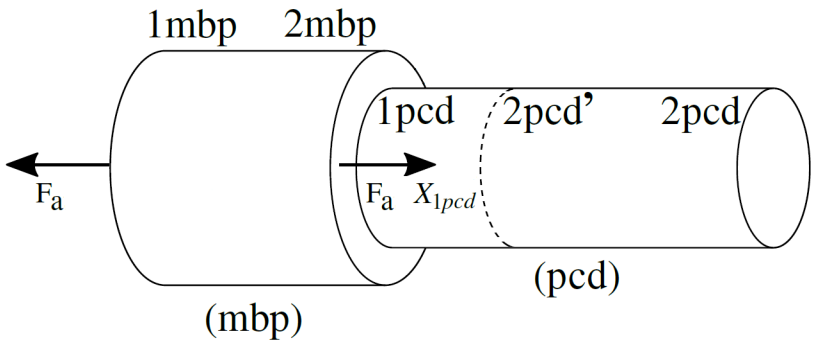

Figure 3.9: Schematic coupling model of subsystems for computation of FRF between sensor voltage and actuation voltage [22]

The compatibility condition is as follows

$$X_{2mbp} = X_{1pcd} \tag{3.33}$$

The following relations hold for equilibrium condition of the forces

$$\begin{aligned} F_{1mbp} &= F_{\mathrm{a}} \\ F_{2mbp} + F_{1pcd} &= -F_{\mathrm{a}} \\ F_{2pcd'} &= 0 \end{aligned} \tag{3.34}$$

The DOF $1pcd$ is the focal point of this formulation. Considering the subsystem *pcd*, the displacement vector $1pcd$ is computed through the following equation

$$X_{1pcd} = H_{1pcd1pcd} F_{1pcd} \tag{3.35}$$

In Eqn.3.35 the force vector F_{1pcd} should be replaced as a function of F_{a} so using

the compatibility condition from Eqn.3.33

$$\begin{aligned} X_{2mbp} = X_{1pcd} &\rightarrow H_{2mbp1mbp}F_{1mbp} + H_{2mbp2mbp}F_{2mbp} = H_{1pcd1pcd}F_{1pcd} \\ &\rightarrow H_{2mbp1mbp}F_{\mathrm{a}} + H_{2mbp2mbp}\left(-F_{1pcd} - F_{\mathrm{a}}\right) = H_{1pcd1pcd}F_{1pcd} \\ F_{1pcd} &= \left(H_{1pcd1pcd} + H_{2mbp2mbp}\right)^{-1}\left(H_{2mbp1mbp} - H_{2mbp2mbp}\right)F_{\mathrm{a}} \end{aligned} \tag{3.36}$$

or

$$F_{1pcd} = gF_{\mathrm{a}}$$

where

$$g = \left(H_{1pcd1pcd} + H_{2mbp2mbp}\right)^{-1}\left(H_{2mbp1mbp} - H_{2mbp2mbp}\right) \tag{3.37}$$

Now substituting F_{1pcd} from Eqn.3.36 into Eqn.3.35,

$$X_{1pcd} = H_{1pcd1pcd}\left(H_{1pcd1pcd} + H_{2mbp2mbp}\right)^{-1}\left(H_{2mbp1mbp} - H_{2mbp2mbp}\right)F_{\mathrm{a}} \tag{3.38}$$

The deflection of the piezoelectric element is related to the measured voltage with the assumption that the sensor voltage is generated only due to displacement at DOF $1pcd$ [22] as:

$$X_{1pcd} = -a\left(F_{1pcd} + bV_s\right) \tag{3.39}$$

where

$$a = \frac{4}{-\rho Al\omega^2 + \frac{\pi^2 A}{lS^E}} \text{and} \quad b = \frac{-\rho Adl\omega^2 + \frac{\pi^2 Ad}{lS^E}}{4} \tag{3.40}$$

here ρ is the density of the piezoelectric material, A is the cross-section area, l is the thickness of the disk, S^E is compliance coefficient ($\frac{m^2}{N}$) and d is the strain constant ($\frac{m}{V}$). Substituting Eq.3.39 into 3.38 and using Eq.3.36 gives

$$\begin{aligned} -a\left(F_{1pcd} + bV_s\right) &= H_{1pcd1pcd}\left(H_{1pcd1pcd} + H_{2mbp2mbp}\right)^{-1}\left(H_{2mbp1mbp} - H_{2mbp2mbp}\right)F_{\mathrm{a}} \\ &\rightarrow -agF_{\mathrm{a}} - abV_s = H_{1pcd1pcd}gF_{\mathrm{a}} \\ \frac{V_s}{F_{\mathrm{a}}} &= -\frac{1}{ab}(H_{1pcd1pcd}g + ag) \end{aligned} \tag{3.41}$$

since the relation between F_{a} and the actuation voltage V_a is given by the equation [22].

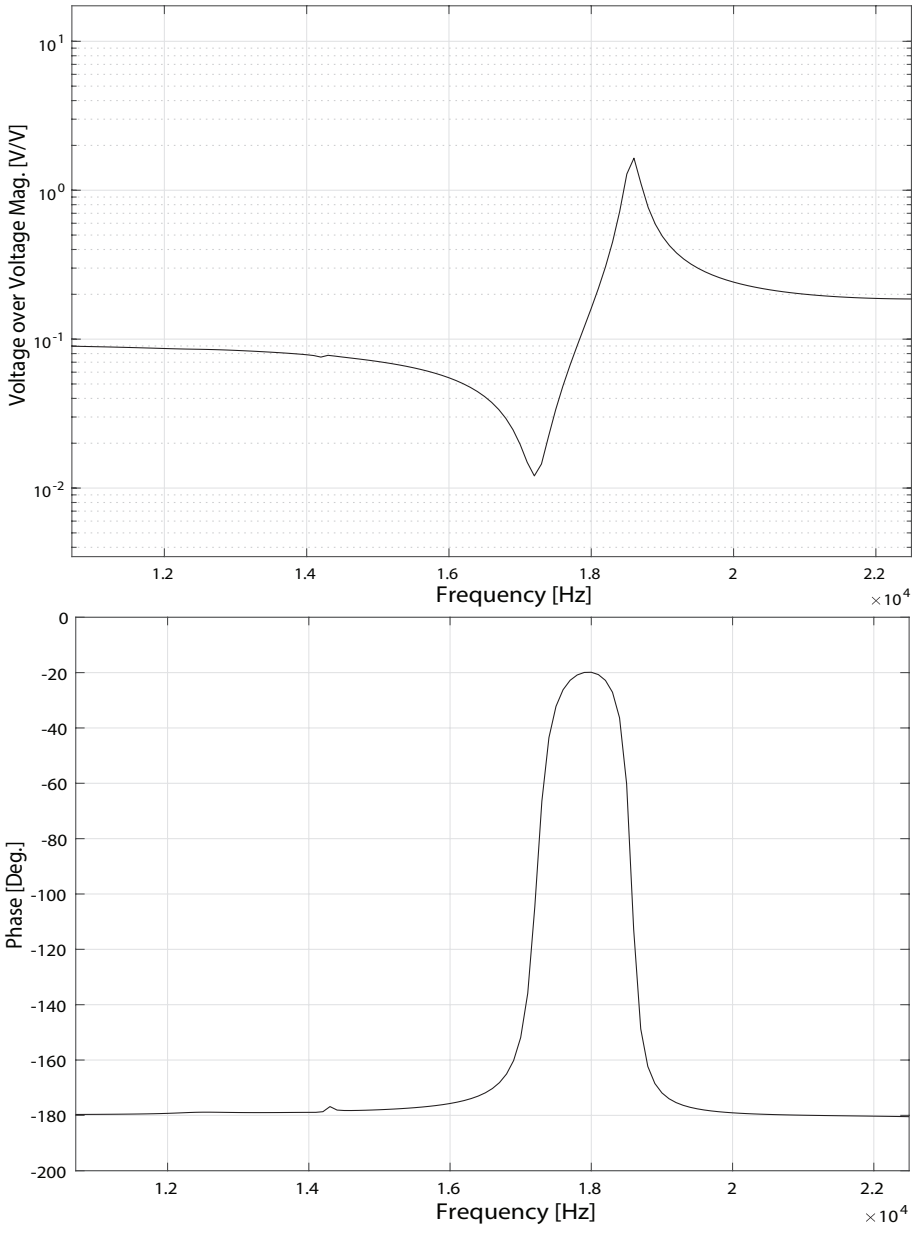

Figure 3.10: FRF between sensor voltage and actuation voltage

$$F_{\mathrm{a}} = \left\{ \frac{Ad}{8}\left(\rho l\omega^2 - \frac{\pi^2}{lS^E}\right) V_a \right\} \tag{3.42}$$

therefore,

$$\frac{V_s}{V_a} = -\frac{Ad}{8}\left(\rho l\omega^2 - \frac{\pi^2}{lS^E}\right)\frac{1}{ab}(H_{1pcd1pcd}g + ag) \tag{3.43}$$

Fig.3.10 shows the resultant FRF obtained using Eqn.3.43

3.3 Validation of SISO models

In the previous sections, the direct and cross single-input-single output (SISO) transfer functions were obtained through receptance coupling of substructures. This section aims to validate theoretical models experimentally and using 3D finite element models developed in a commercial software (COMSOL Multiphysics). The FRFs (V_s/F) and (V_s/V_a) are validated experimentally, whereas the FRFs (θ/F), (z/T), (θ/T) and (θ/V_a) are validated using the software. The purpose of these validation tests is to ensure that direct and cross axial as well as torsional FRFs are correct.

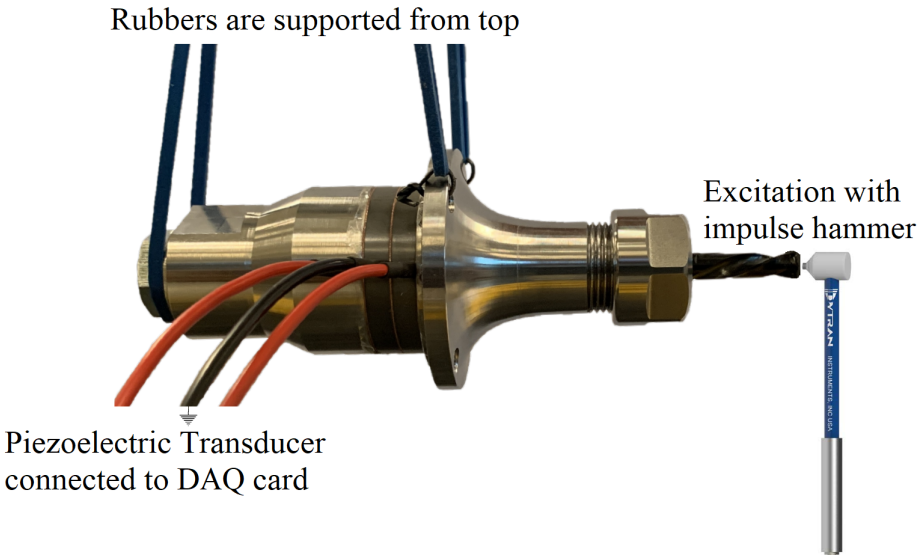

Figure 3.11: Experimental setup to validate FRF (V_s/F) [22]

The FRF between sensor voltage V_s and force F is validated by performing impulse-hammer test. An impulse force is applied at the tip of the drill bit with

VAD system in free-free boundary conditions, using an instrumented hammer (Dytran 5800SL). The resulting piezolectric sensor voltage is measured using NI compact (cDAQ-9234) data acquisition card as shown in Fig.3.11. A lightweight impulse hammer is used because its low inertia enables quicker rebounding hence produces a very high frequency excitation. The excitation and response is measured at 51200 Hz sampling frequency and the corresponding FRF is obtained using the power spectral densities of the excitation and response signal [8]. Fig.3.12 shows the resulting FRFs.

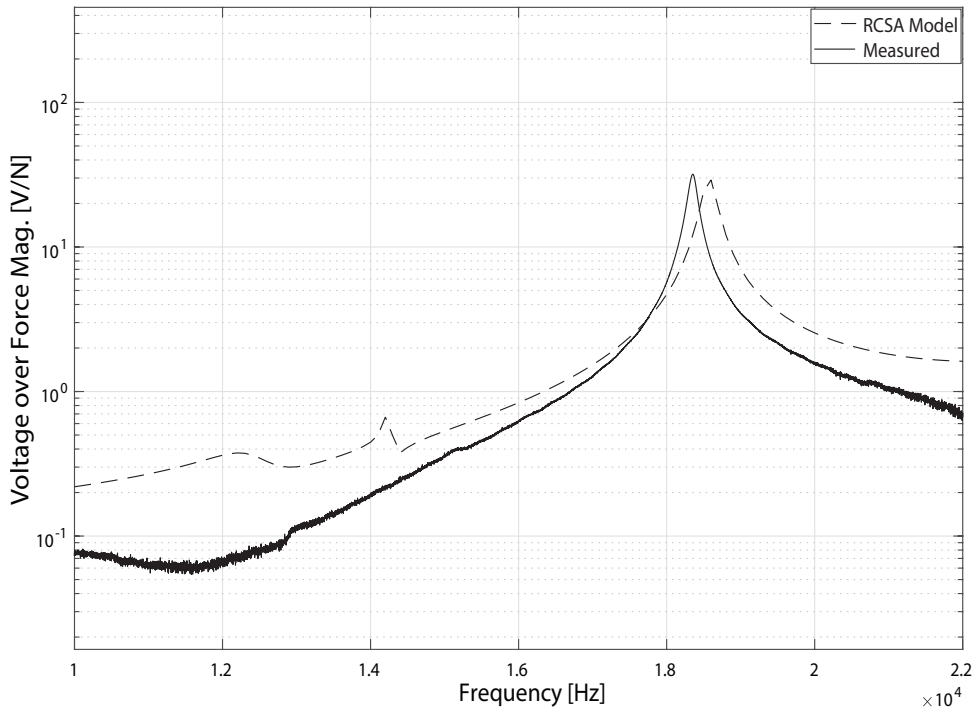

Figure 3.12: Comparision of FRFs (V_s/F) obtained experimentally and from RCSA modelling

Validation of transfer function between sensor voltage and actuation voltage is also performed experimentally and a sinesweep voltage between 0.2 kHz and 25 kHz is applied at the piezoelectric actuator and the voltage response is measured from the piezoelectric sensor as shown in Fig.3.13. Excitation of the VAD system is performed in free-free boundary conditions by applying a voltage with 11 V amplitude and an increasing frequency with the rate of 11 octaves/min using a function generator (RS PRO IFG8216A). The excitation and response is measured at 51200 Hz sampling frequency and the corresponding FRF is obtained using the power spectral densities

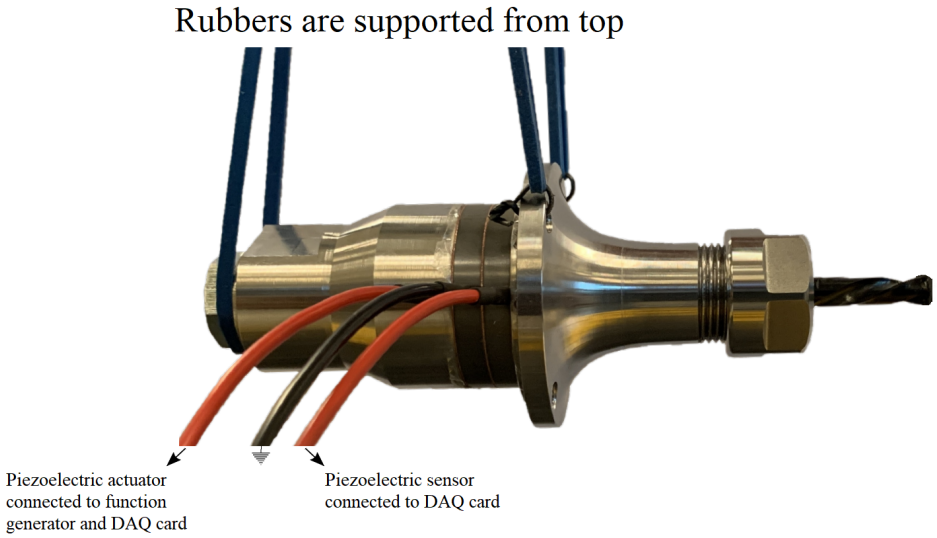

Figure 3.13: Experimental setup to validate FRF (V_s/V_a) [22]

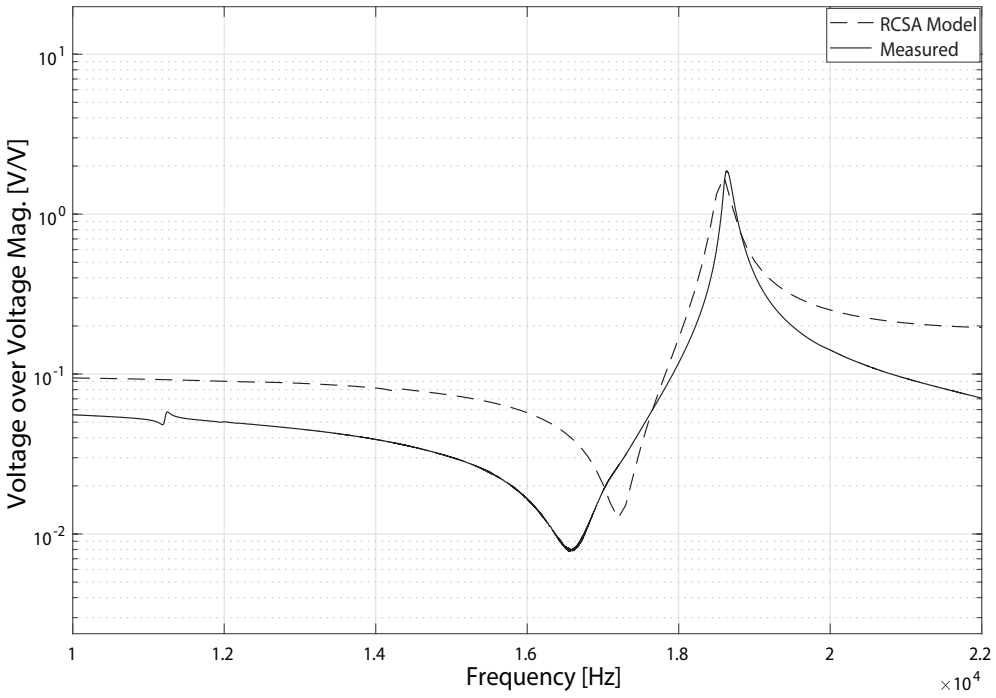

Figure 3.14: Comparision of FRFs (V_s/V_a) obtained experimentally and from RCSA modelling

of the excitation and response signal. Fig.3.14 shows the resulting FRFs.

The transfer functions (θ/T) and (z/T) obtained from the RCSA model are compared to those obtained from Comsol Multiphysics platform. The VAD system is modelled in the solid mechanics module of software, with a physics-controlled meshing sequence and fine mesh element size as shown in Fig.3.15. The excitation to the

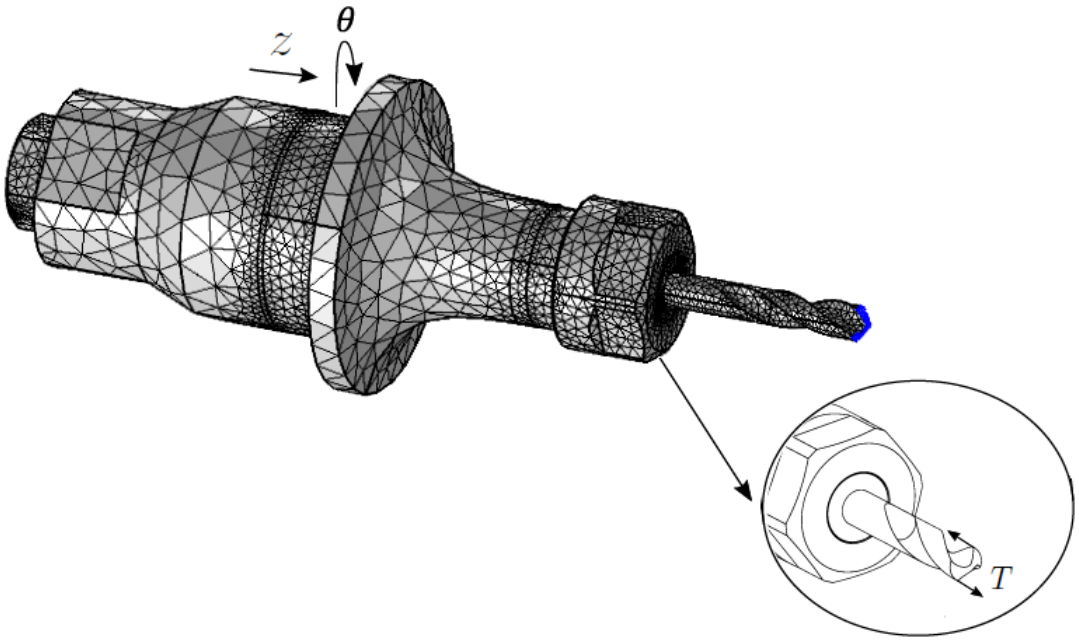

Figure 3.15: Excitation and measurement of VAD system in COMSOL to determine FRFs (θ/T) and (z/T)

system is torque applied at the tip of the drill bit while axial displacement and torsional deflection are measured at the piezodisk-concentrator joint. Fig.3.16 shows the VAD system's torsional and axial receptance at piezodisk-concentrator joint obtained from the RCSA model compared against the receptances of the 3D model computed by the finite element software. The mode shape (around 14 kHz) of the resonance peak in the resulting FRFs is shown in Fig.3.17 which suggest that the torsional load at the tip of the drill bit is generating substantial torsional motion at the tip of the drill bit.

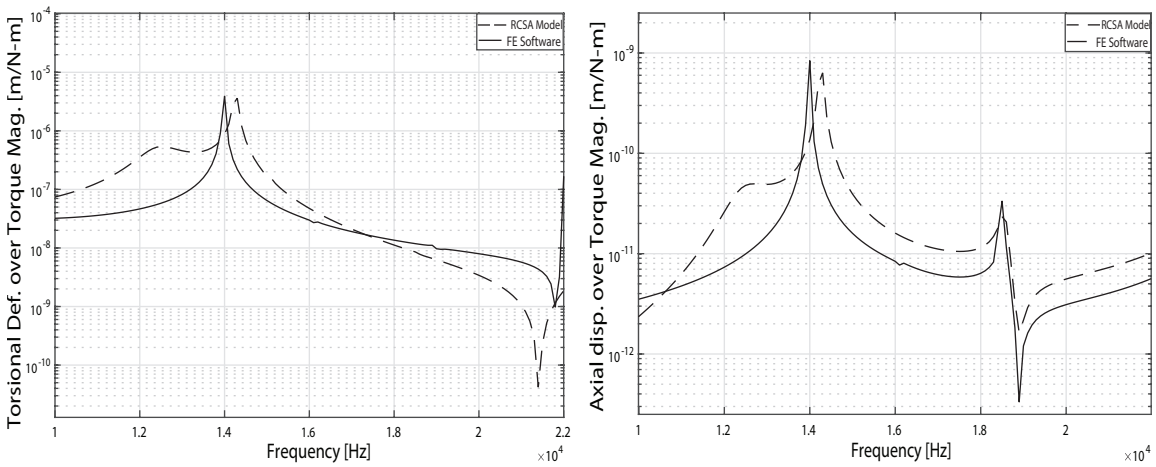

Figure 3.16: Comparision of FRFs (θ/T) and (z/T) obtained from RCSA and FEM modelling

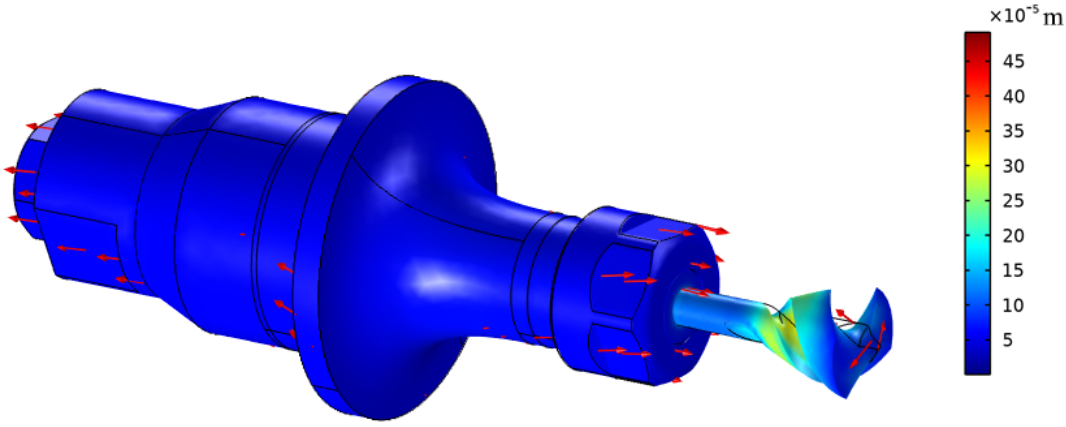

Figure 3.17: Mode shape of VAD system due to torsional load obtained in 3D FEM in COMSOL Multiphysics

The transfer function (θ/V_a) obtained from the RCSA model is also compared to the one obtained from Comsol Multiphysics platform. The VAD system is modelled in the solid mechanics module of software, with a physics-controlled meshing sequence and fine mesh element size as shown in Fig.3.18. The excitation to the assembly is actuation voltage represented by a pair of opposite-direction distributed forces applied at each end of piezoelectric transducer, whereas the torsional deflection is measured at the piezodisk-concentrator joint shown in Fig.3.18. The VAD system's

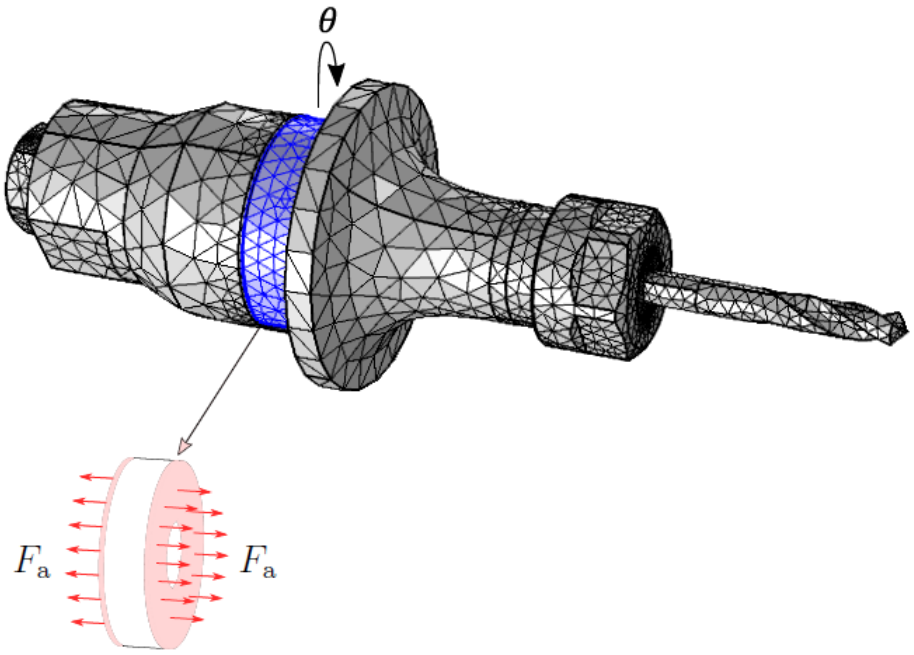

Figure 3.18: Excitation and measurement of VAD system in COMSOL to determine FRF (θ/F_a)

torsional receptance at piezodisk-concentrator joint obtained from the RCSA model is compared against the receptance of the 3D model computed by the finite element software shown in Fig.3.19. The mode shape (around 18 kHz) of the resonance peak in the resulting FRFs is shown in Fig.3.20 which suggest that the actuation voltage at the piezoelectric transducer is generating strong axial motion which is amplified at the drill bit.

For the validation of transfer function (θ/F), VAD system is modelled in the solid mechanics module of software, with a physics-controlled meshing sequence and fine mesh element size as shown in Fig.3.21. The excitation to the system is force applied at the tip of the drill bit and torsional deflection is measured at the piezodisk-

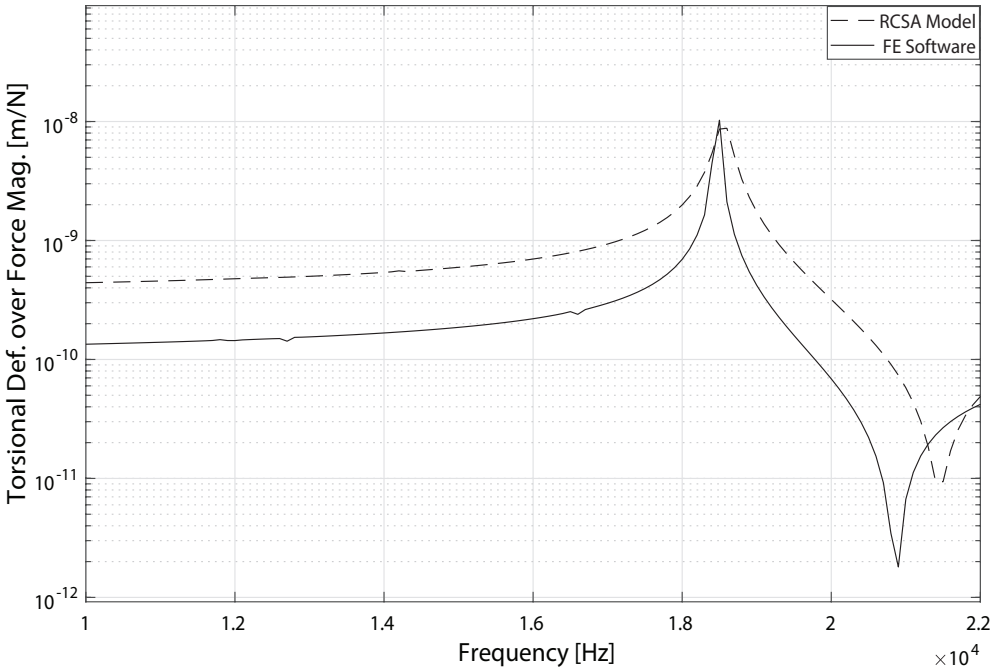

Figure 3.19: Comparision of FRFs (θ/F_a) obtained from RCSA and FEM modelling

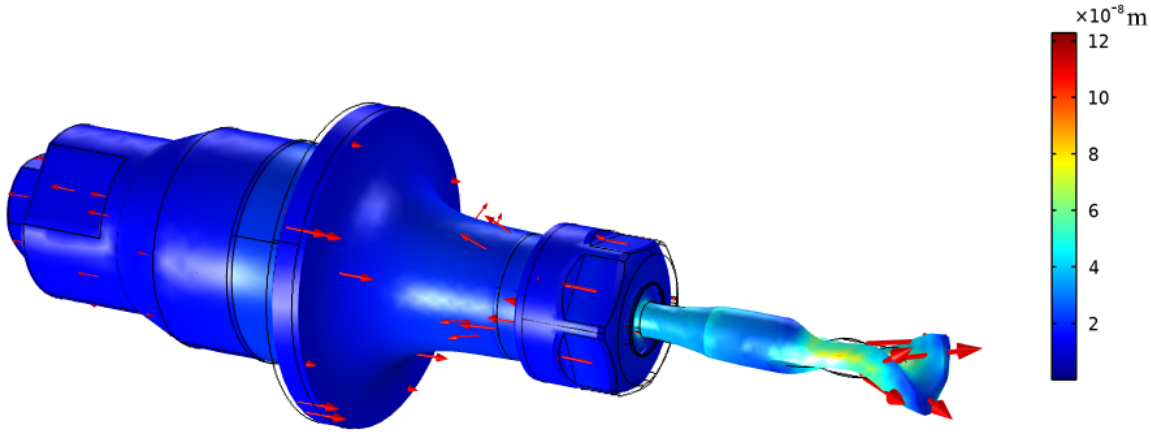

Figure 3.20: Mode shape of VAD system due to actuation voltage obtained in 3D FEM in COMSOL Multiphysics

concentrator joint. The VAD system's torsional receptance at piezodisk-concentrator joint obtained from the RCSA model is compared against the receptance of the 3D model computed by the finite element software shown in Fig.3.22. The mode shape

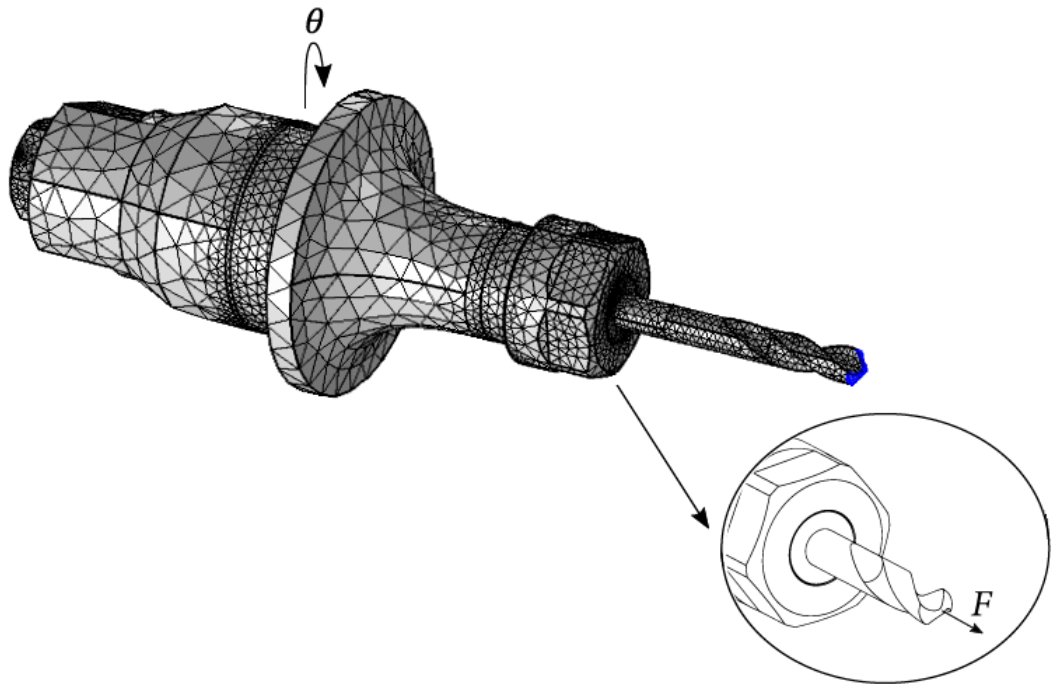

Figure 3.21: Excitation and measurement of VAD system in COMSOL to determine FRF (θ/F)

(around 14 kHz) of the resonance peak in the resulting FRFs is shown in Fig.3.23 which suggest that the axial load at the tip of the drill bit is generating substantial axial motion throughout the drill bit.

The comparison of the receptance plots resulting from RCSA method, 3D FEM and experiments show that both axial and torsional receptance functions are accurately predicted in the operating frequency range of VAD system.

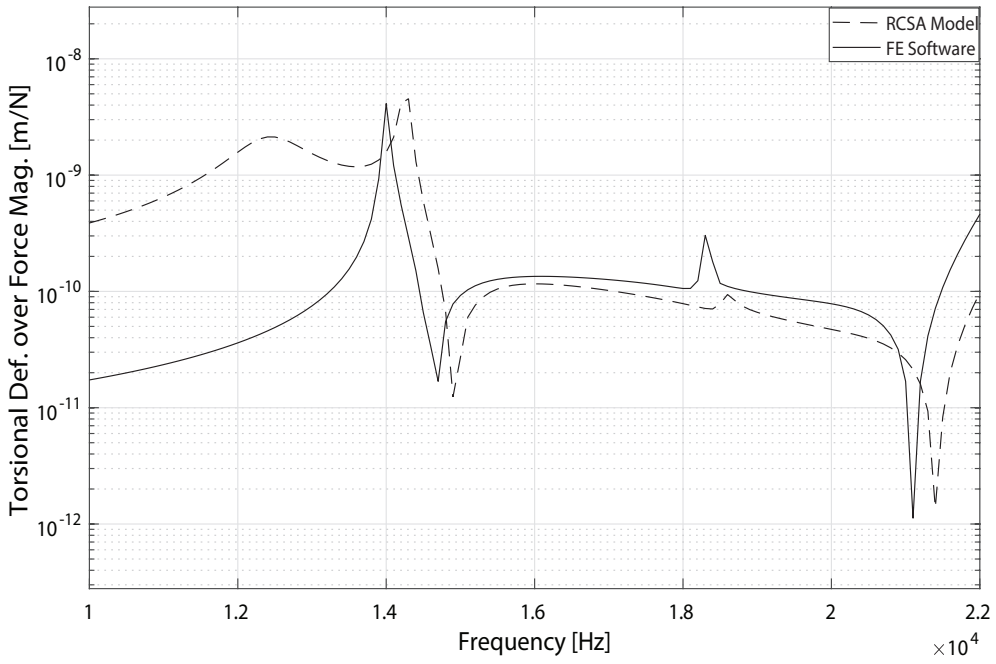

Figure 3.22: Comparision of FRFs (θ/F) obtained from RCSA and FEM modelling

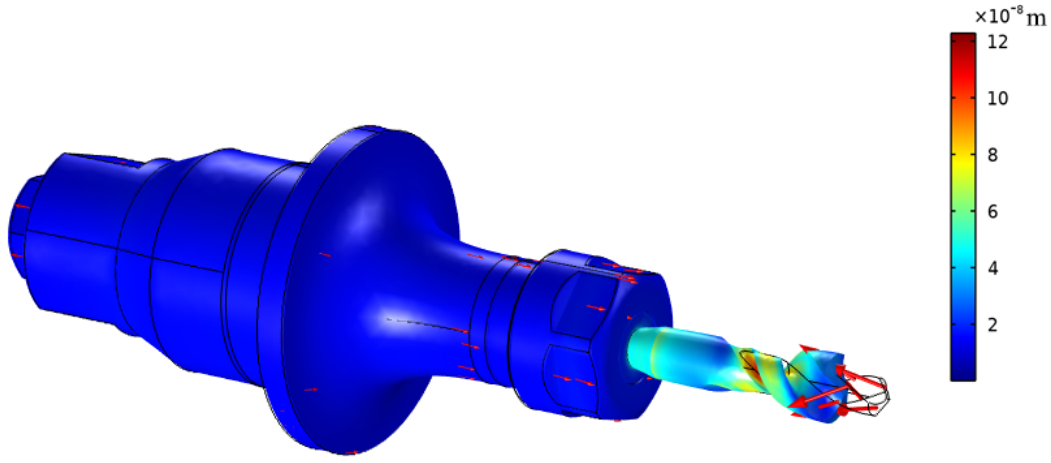

Figure 3.23: Mode shape of VAD system due to axial force at drill bit obtained in 3D FEM in COMSOL Multiphysics

3.4 System identification

Based on the six single-input-single-output FRFs, an overall MIMO parametric system model is obtained using a Matlab tool which computes eigenfrequency, modal damping ratio and complex residues [6]. This tool uses linear square complex frequency estimator (LSCF) to identify eigenfrequency and modal damping, whereas the modal residues are estimated using least-squares frequency-domain estimator (LSFD). The identified model is represented by three modes shown in Table 3.2.

Eigenfrequency ω_n and modal damping ζ is used for the identification of system poles and then using complex residues a Pole-Residue model is developed using the following equations.

$$h_{mn}(s) = \sum_{r=1}^{N_m} \frac{R_{mn,r}}{s - p_r} + \sum_{r=1}^{N_m} \frac{R^*_{mn,r}}{s - p^*_r} \tag{3.44}$$

$$p_r, p^*_r = -\zeta\omega_n \pm \mathrm{i}\omega_n\sqrt{1-\zeta^2} \tag{3.45}$$

In Eq.3.44, the subscript m is for output voltage V_s and torsional displacement θ, whereas subscript n is for input force F, torque T and actuation voltage V_a with p_r and $R_{mn,r}$ respectively the poles and residue matrices as model parameters corresponding to the r^{th} mode of the structure. The continuous time SISO systems generated by Eq.3.44 are described by the following transfer function:

$$h_{mn}(s) = \frac{b_1 s^{n-1} + b_2 s^{n-2} + \ldots + b_n}{s^n + a_1 s^{n-1} + \ldots + a_n} \tag{3.46}$$

The MIMO transfer function model structure characterizing system dynamics and relating the three inputs with the two outputs is formulated using SISO transfer functions as

$$H(s) = \begin{bmatrix} h_{V_sF} & h_{V_sT} & h_{V_sV_a} \\ h_{\theta F} & h_{\theta T} & h_{\theta V_a} \end{bmatrix} \tag{3.47}$$

Estimated parameters of the sixth order transfer function model in continuous-time with respect to each output are given in Table 3.3. The state-space model of the VAD is obtained by mapping the transfer function in Eq.3.47 to companion-form state-space model as follows:

Table 3.2: Modal Parameters

Mode	Frequency [Hz]	Damping ratio [%]
1	12446	0.0397
2	14259	0.0023
3	18560	0.0052

$$\begin{aligned} \{\dot{x}_c(t)\} &= [A_c]\{x_c(t)\} + [B_c]\begin{Bmatrix} F(t) \\ T(t) \\ V_a(t) \end{Bmatrix} \\ \begin{Bmatrix} V_s(t) \\ \theta(t) \end{Bmatrix} &= [C_c]\{x_c(t)\} \end{aligned} \tag{3.48}$$

where $\{x_c\}(t) = [x_1(t), ..., x_n(t)]^T$ is the state vector, $[A_c]$ is the companion form system matrix, and $[B_c]$ and $[C_c]$ are the corresponding input and output distribution matrices, respectively, expressed in terms of the transfer function coefficients [18]:

$$[A_c] = \begin{bmatrix} 0 & I_p & 0 & & 0 \\ 0 & 0 & I_p & \ddots & 0 \\ & & \ddots & \ddots & 0 \\ 0 & 0 & 0 & & I_p \\ -a_n I_p & \cdots & -a_3 I_p & -a_2 I_p & -a_1 I_p \end{bmatrix}; [B_c] = \begin{bmatrix} 0 \\ 0 \\ \vdots \\ I_p \end{bmatrix}; [C_c] = \begin{bmatrix} b_n \\ \vdots \\ b_2 \\ b_1 \end{bmatrix} \tag{3.49}$$

where I_p is identity matrix with its dimension equal to number of inputs p. The state-space model given in Eq.3.48 is finally discretized using Zero-Order-Hold (ZOH) discretization with a sampling rate Δt=1/51200 sec as follows:

$$\begin{aligned} \{x(k+1)\} &= [A]\{x(k)\} + [B]\begin{Bmatrix} F(k) \\ T(k) \\ V_a(k) \end{Bmatrix} \\ \begin{Bmatrix} V_s(k) \\ \theta(k) \end{Bmatrix} &= [C]\{x(k)\} \end{aligned} \tag{3.50}$$

Table 3.3: Estimated parameters of sixth order continuous time transfer function model

h_{V_sF}	$\frac{-1615s^5-4.333e09s^4-6.097e13s^3-6.136e19s^2-3.803e23s-2.131e29}{s^6+7834s^5+2.775e10s^4+1.596e14s^3+2.415e20s^2+7.716e23s+6.675e29}$
h_{V_sT}	$\frac{-134.5s^5-4.201e07s^4-2.853e12s^3-7.358e17s^2-1.382e22s-1.823e27}{s^6+7834s^5+2.775e10s^4+1.596e14s^3+2.415e20s^2+7.716e23s+6.675e29}$
$h_{V_sV_a}$	$\frac{101.3s^5+2.345e08s^4+3.304e12s^3+3.292e18s^2+1.975e22s+1.13e28}{s^6+7834s^5+2.775e10s^4+1.596e14s^3+2.415e20s^2+7.716e23s+6.675e29}$
$h_{\theta F}$	$\frac{7893s^5+4.111e09s^4+1.867e14s^3+9.261e19s^2+1.052e24s+5.032e29}{s^6+7834s^5+2.775e10s^4+1.596e14s^3+2.415e20s^2+7.716e23s+6.675e29}$
$h_{\theta T}$	$\frac{1.173e06s^5+2.217e11s^4+2.524e16s^3+1.375e21s^2+1.214e26s-2.241e31}{s^6+7834s^5+2.775e10s^4+1.596e14s^3+2.415e20s^2+7.716e23s+6.675e29}$
$h_{\theta V_a}$	$\frac{41.69s^5-1.21e08s^4-6.218e10s^3-1.731e18s^2-3.116e21s-6.097e27}{s^6+7834s^5+2.775e10s^4+1.596e14s^3+2.415e20s^2+7.716e23s+6.675e29}$

where $x(k)$=$x(k\Delta t)$, $\{F(k)\ T(k)\ V_a(k)\}^T = \{F(k\Delta t)\ T(k\Delta t)\ V_a(k\Delta t)\}^T$ and $\{V_s(k)\ \theta(k)\}^T = \{V_s(k\Delta t)\ \theta(k\Delta t)\}^T$. The discrete-time input distribution matrices, $[A]$ and $[B]$, are defined as follows:

$$[A] = e^{A_c\Delta t}; \quad [B] = \int_0^{\Delta t} e^{A_c\Delta t}[B_c]dt \tag{3.51}$$

As shown in Fig.3.24 for the model validation, FRFs obtained from RCSA model (dashed-line) are compared with the estimated FRFs (solid-line) generated by Matlab tool. The agreement is acceptable and the model structure for an observer design is adequate for obtaining estimated cutting force results.

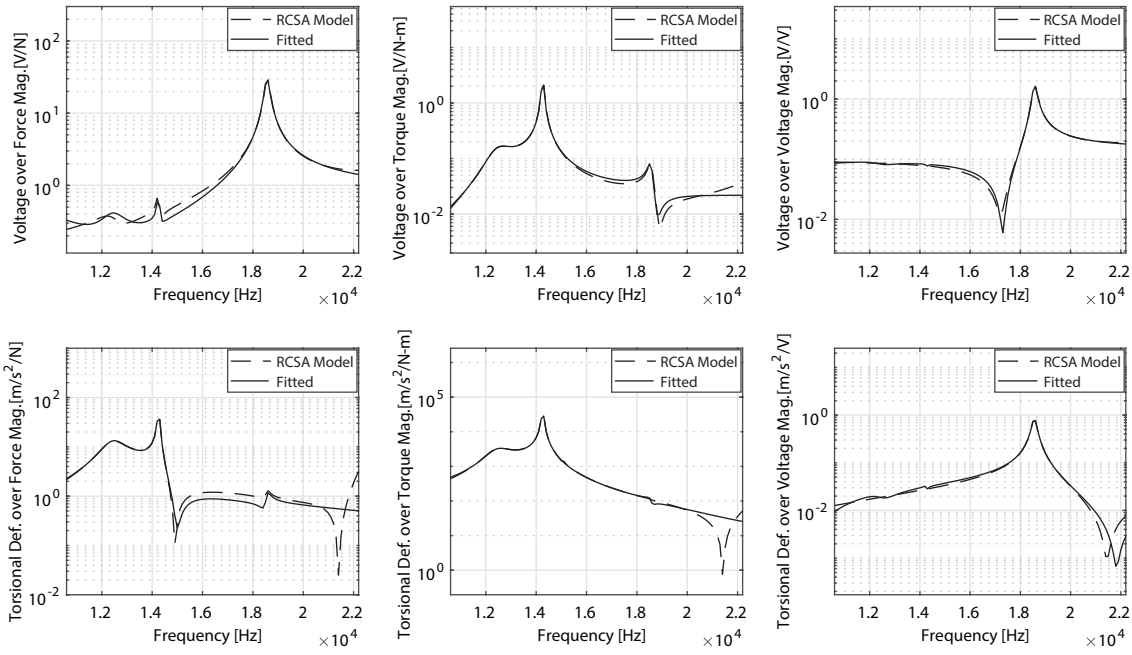

Figure 3.24: Modelled and identified FRFs between input and output signals

Chapter 4

Cutting Force Reconstruction on VAD System

4.1 Introduction

In this chapter, the Kalman Filter is used to estimate the axial thrust force and torque from the voltage signal measured from the piezoelectric sensor embedded in VAD system and the torsional deflection measured by the piezoelectric accelerometer. The axial cutting force is then validated by comparing it against the force measurements obtained from the load cell.

4.2 Experimental setup

Configuration of the actuation voltage, force, and sensor signal measurement setup is shown in Fig.4.1. One of the inputs to this system is known AC voltage provided to piezoelectric actuator in order to excite VAD system around its resonance frequency. The other two inputs are axial thrust force and torque generated at the tip of drill bit. The axial displacement is measured in the form of voltage obtained from the piezoelectric sensor whereas the torsional deflection is measured using an accelerometer (PCB 352C22, sensitivity 10.42 $\frac{mV}{g}$) which is placed near the piezodisk-concentrator joint. Since the tip of the drill bit is not flat, a coupler is designed to attach it to a force sensor (PCB 208C01) as shown in Fig.4.1. The input and output signals are discretized using NI compact (cDAQ-9234) data acquisition card and stored in a PC. A sampling rate of 51200 Hz is used.

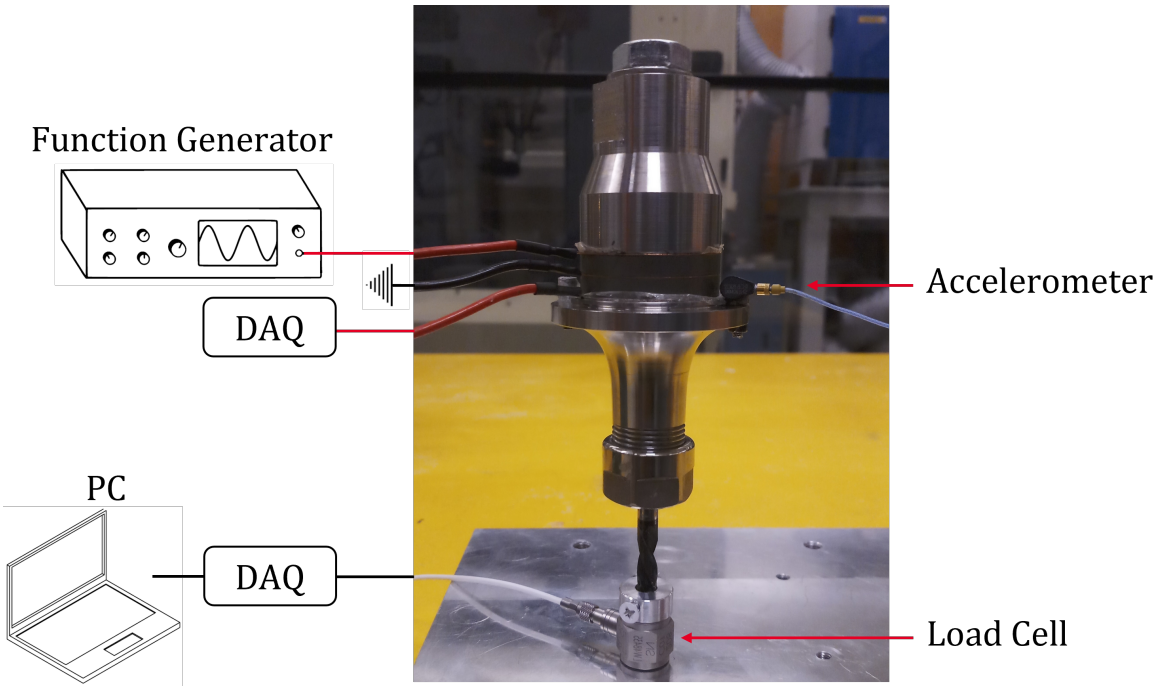

Figure 4.1: The experimental setup

The AC voltage supplied to piezoelectric actuator is generated by a function generator (RS PRO IFG8216A) and is in range of -11 to +11 volts. The voltage signal generated by piezoelectric sensor at resonance frequency is around -100 to +100 volts. The NI DAQ card can only tolerate voltages in the range of -5 to +5 volts. Therefore, the terminals of piezoelectric actuator and sensor can not be directly connected to the DAQ card channels for voltage measurement. So in order to bring this voltage to the range of DAQ card measurement, a voltage divider circuit is employed.

The voltage divider circuit is shown in Fig.4.2. The voltage across piezoelectric actuator V_{pa} and piezoelectric sensor V_{ps} will damage the DAQ card if connected directly to its channels. The voltage V_{ma} and V_{ms} measured by the DAQ card is computed using the following relations which are based on voltage divider circuits shown in Fig.4.2.

$$V_{ma} = \frac{R_1}{R_1 + R_2} V_{pa} \rightarrow V_{ma} = \frac{10}{10 + 56} V_{pa} = \frac{1}{6.6} V_{pa} \tag{4.1}$$

$$V_{ms} = \frac{R_3}{R_3 + R_4} V_{ps} \rightarrow V_{ms} = \frac{10}{10 + 284} V_{ps} = \frac{1}{29.4} V_{ps} \tag{4.2}$$

Based on Eq.4.1 and Eq.4.2, the dropped voltages V_{ma} and V_{ms} are now brought to

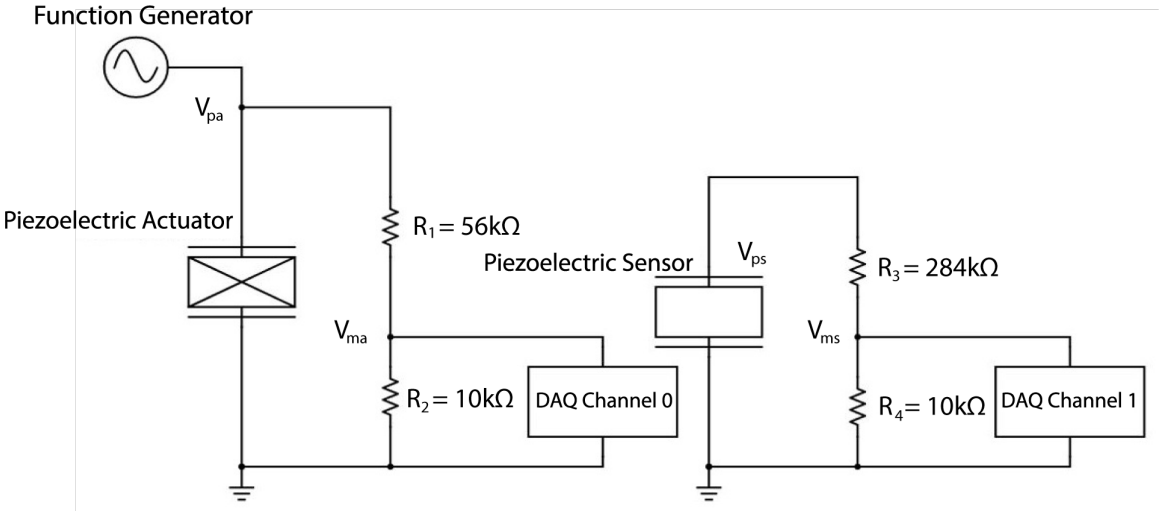

Figure 4.2: Measuring voltage from piezoelectric actuator and sensor

the range of -1.67 to +1.67 volts of V_{pa} and -3.4 to +3.4 of V_{ps} respectively. These voltage ranges are safe to be connected to Channel 0 and 1 of the DAQ card.

4.3 Inverse force and torque estimation based on MIMO model

For the inverse force and torque estimation, Kalman Filter is applied to augmented state space model given by equation

$$\{\hat{x}_a(k+1)\} = [A_a]\{\hat{x}_a(k)\} + [B_{v_a}]V_a(k) \tag{4.3}$$

where

$$\{\hat{x}_a(k)\} = \begin{Bmatrix} x(k) \\ F(k) \\ T(k) \end{Bmatrix}; [A_a] = \begin{bmatrix} A & B_{n\times 2} \\ 0_{2\times n} & I_2 \end{bmatrix} \tag{4.4}$$

here, $B_{n\times 2}$ contains the first two column and B_{v_a} contains the third column of input distribution matrix B. The output vector is also expressed in terms of augmented state vector and augmented measurement matrix as

$$\begin{Bmatrix} \hat{V}_s \\ \hat{\theta} \end{Bmatrix} = [C_a]\{\hat{x}_a(k)\} \tag{4.5}$$

The estimated augmented state is obtained from the output measurements V_s and θ using the following Kalman filter observer

$$\begin{aligned} \{\hat{x}_a(k)\}^- &= [A_a]\,\{\hat{x}_a(k-1)\}^+ + [B_{v_a}]\,V_a(k) \\ \{\hat{x}_a(k)\}^+ &= \{\hat{x}_a(k)\}^- + \{L(k)\}\left(\left\{\begin{array}{c} V_s \\ \theta \end{array}\right\} - [C_a]\,\{\hat{x}_a(k)\}^-\right) \end{aligned} \tag{4.6}$$

In the steady state with constant kalman gain $\{L_\infty\}$, the observer is described by the following model:

$$\begin{aligned} \{\hat{x}_a(k)\}^+ = &([A_a] - \{L_\infty\}\,[C_a]\,[A_a])\,\{\hat{x}_a(k-1)\}^+ \\ &+ [\{L_\infty\} \quad ([B_{v_a}] - \{L_\infty\}\,[C_a]\,[B_{v_a}])] \left\{\begin{array}{c} V_s \\ \theta \\ V_a \end{array}\right\} \\ &\left\{\begin{array}{c} \hat{F}(k) \\ \hat{T}(k) \end{array}\right\} = \left[\bar{C}_a\right]\{\hat{x}_a(k)\}^+ \end{aligned} \tag{4.7}$$

where $\left[\bar{C}_a\right] = [0_{2\times n}\ I_2]$. The transfer function of Kalman Filter system described in Eq.4.7, depends on system model described by the matrices $[A_a]$, $[B_{v_a}]$, $[C_a]$ and the steady state Kalman gain L_∞, which depends on process noise covariance matrix $[Q]$, measurement noise covariance matrix $[R]$, and force regularization matrix $[S]$. Measurement noise covariance matrix $[R]$ is determined by computing the covariance of sensor signals when no actuation voltage is applied and VAD system is in free-free boundary conditions. The process noise covariance matrix $[Q]$ is a scalar matrix with equal diagonal values, which depend on modelling errors and uncertainty in system dynamics. The measurement noise covariance matrix $[R]$ and force regularization matrix $[S]$ are represented in Eq.2.14. The regularization factors S_f and S_t are used to regularize noise magnification due to the ill-conditioning of the inverse force reconstruction problem. When it is assumed that there is no noise present in measurement signals (i.e. $[R] = 0$), then regularization factors are turned off and the transfer functions of Kalman Filter system represented as dashed-line in Fig.4.3, tend to compensate the system dynamics.

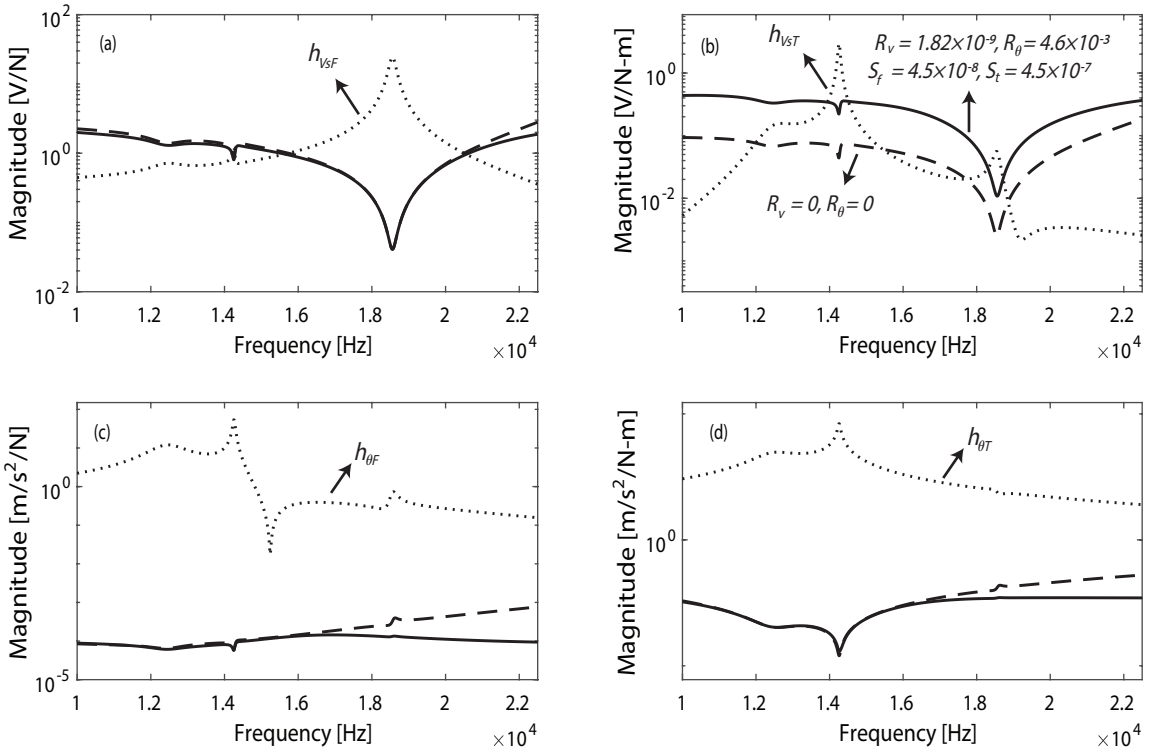

Figure 4.3: Kalman filter transfer functions (a) h_{V_sF}, (b) h_{V_sT} (c) $h_{\theta F}$ and (d) $h_{\theta T}$

4.4 Force identification

The force identification process consists of a series of experimental tests which are performed at discrete frequencies ranging from 12 kHz to 22 kHz. In all the tests, only the comparison between the experimentally measured and estimated thrust force is made.

With the assumption that there are no modelling errors, the diagonal values of process noise covariance matrix are set to $[Q] = 0$, whereas the computed covariances of sensor voltage noise and accelerometer signal noise are $R_v = 1.82 \times 10^{-9}\ V^2$ and $R_\theta = 4.6 \times 10^{-3}\ (\frac{m}{s^2})^2$, respectively. The optimum values of regularization factors are determined by plotting the output estimation error norms and smoothing norms against the regularization factors. For any value of S_f and S_t , the sensor voltage output estimation error and force smoothing error norms at each timestep are defined as, $\left\|\left\{\hat{V}_s(k)\right\} - \{V_s(k)\}\right\|$ and $\left\|\left\{\hat{F}(k)\right\}\right\|$, respectively, wherease the torsional deflection estimation error and torque smoothing error norms are defind as $\left\|\left\{\hat{\theta}(k)\right\} - \{\theta(k)\}\right\|$ and $\left\|\left\{\hat{T}(k)\right\}\right\|$, respectively. Fig.4.4 shows the variation of estimation error and

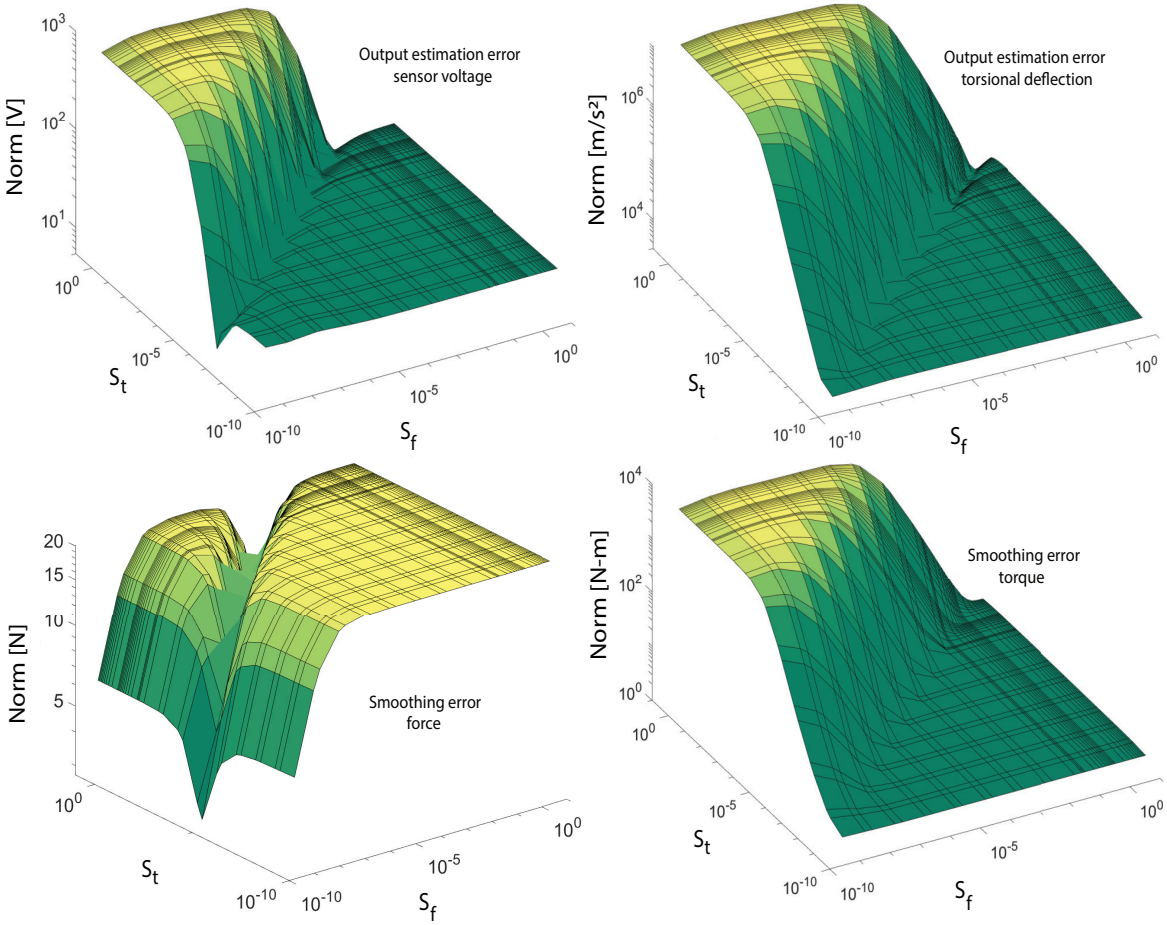

Figure 4.4: Variation of output estimation and smoothing error norms when regularization gains S_f and S_t varies between 10^{-10} and 10^{0}.

smoothing norms when the force and torque regularization factors in the AKF algorithm varies between 10^{-10} and 10^{0}. It is observed that for a certain value of S_t, increment in S_f factor cause the estimation errors to reduce, while this approach of tuning cause the force smoothing norm to increase, indicating noise magnification in estimated force. On the other hand it causes the torque smoothing to decrease, indicating smoothing of estimated torque. For a few values of S_t, increase in S_f result in high force smoothing norm which then abruptly decline and then increase. When S_t is increased while S_f remains constant, the torque smoothing norm increases while the force smoothing norm remains unchanged, indicating noise magnification in estimated torque only. As a result, it can be concluded that the factor S_f affects the smoothing of both estimated force and torque, whereas the factor S_t mainly affects the smoothing of estimated torque. Since any combination of S_f and S_t near the

valley of the output estimation error surface plots will result in the least amount of error, they are picked near the valleys. The optimum determined values of force and torque regularization factors are $S_f = 4.5 \times 10^{-8}\ N^2$ and $S_t = 4.5 \times 10^{-7}\ (N.m)^2$, respectively. The Kalman Filter transfer functions obtained using these regularization factors are shown with solid line in Fig.4.3.

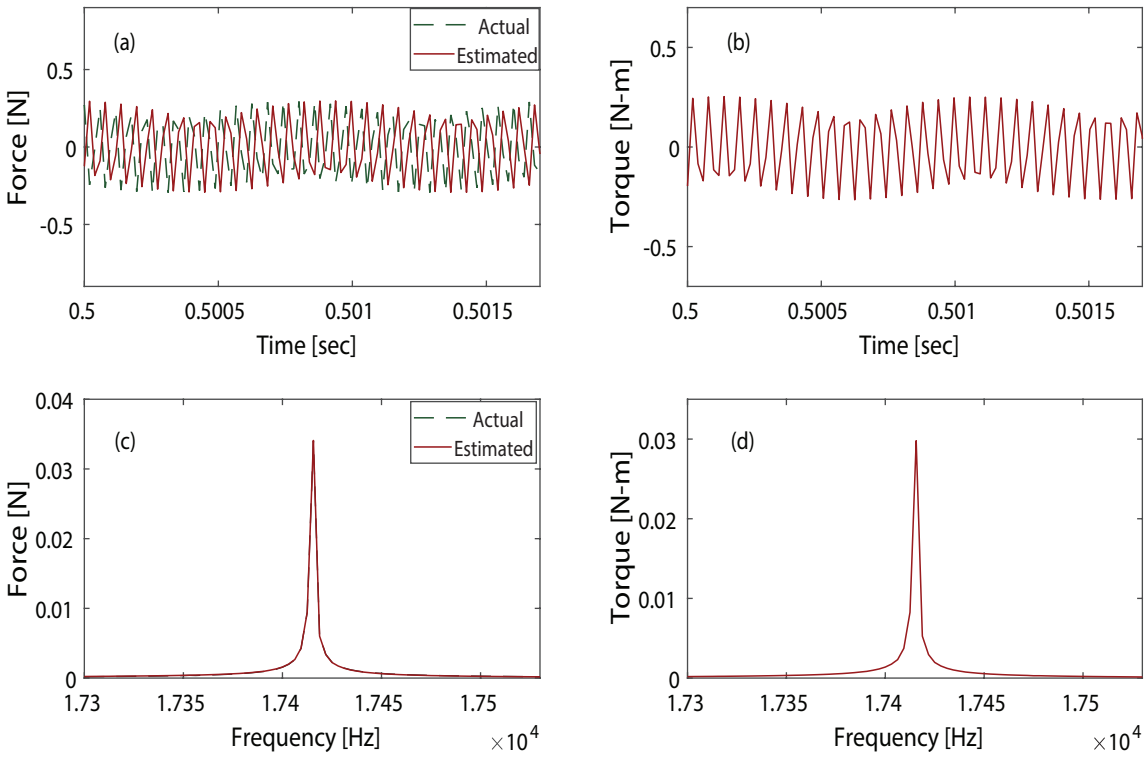

Figure 4.5: (a) Measured and reconstructed forces using Augmented Kalman Filter Method at around 18 kHz. (b) Reconstructed torque using Augmented Kalman Filter Method. (c) FFT of measured and reconstructed forces. (d) FFT of the reconstructed torque. Measured force is shown with dotted line and reconstructed force is shown with solid line.

Fig.4.5 report the input estimation results obtained using optimum regularization factors, when VAD system is actuated with a voltage signal of around 18 kHz. It is evident in Fig.4.5 that Augmented Kalman Filter (AKF) is able to deliver very accurate estimate of measured actual axial force time history. The FFT of the actual and estimated forces feature a peak corresponding to the frequency of actuation voltage.

In another case, actuation voltage of around 12 kHz and 13 kHz is applied at the piezoelectric actuator. Figures 4.6 and 4.7 show the estimated force and torque

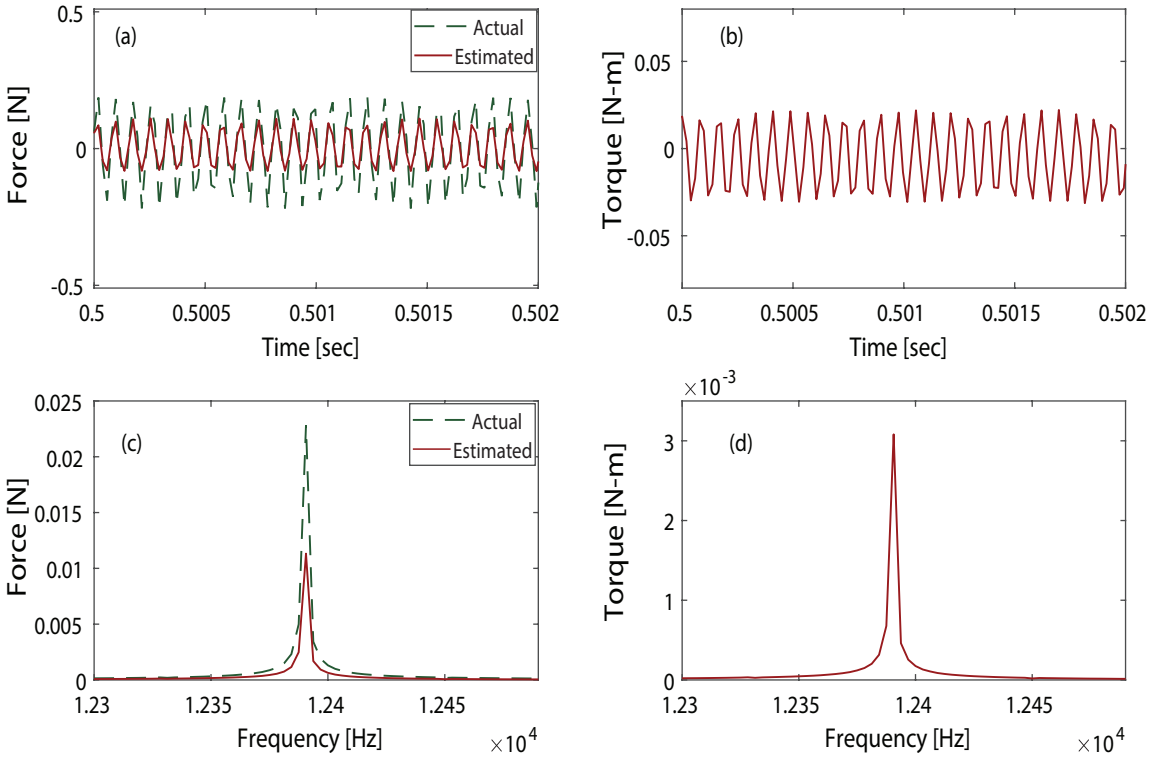

Figure 4.6: (a) Measured and reconstructed forces using Augmented Kalman Filter Method at around 12 kHz. (b) Reconstructed torque using Augmented Kalman Filter Method. (c) FFT of measured and reconstructed forces. (d) FFT of the reconstructed torque. Measured force is shown with dotted line and reconstructed force is shown with solid line.

which are reconstructed using the voltage signal from the piezoelectric sensor and torsional deflection from the accelerometer. It is observed that AKF is able to deliver sufficiently accurate estimate of actual force time history. However, the magnitude of estimated axial force is slightly lower as compare to the case when frequency of response signals is around 18 kHz. The slight discrepancy in estimation result is due to the fact that overall gain of axial mode at 14 kHz is considerably lower than 18 kHz mode, resulting in slightly weaker output signal which is being used by AKF to estimate input signal. The FFTs of the actual and estimated forces feature peaks corresponding to the frequency of actuation voltage.

A case is also considered in which frequency of actuation voltage is around 16 kHz. Fig.4.8 illustrate the estimations of axial force and torque. It is observed that AKF is able to provide quite accurate estimate of measured actual axial force time history.

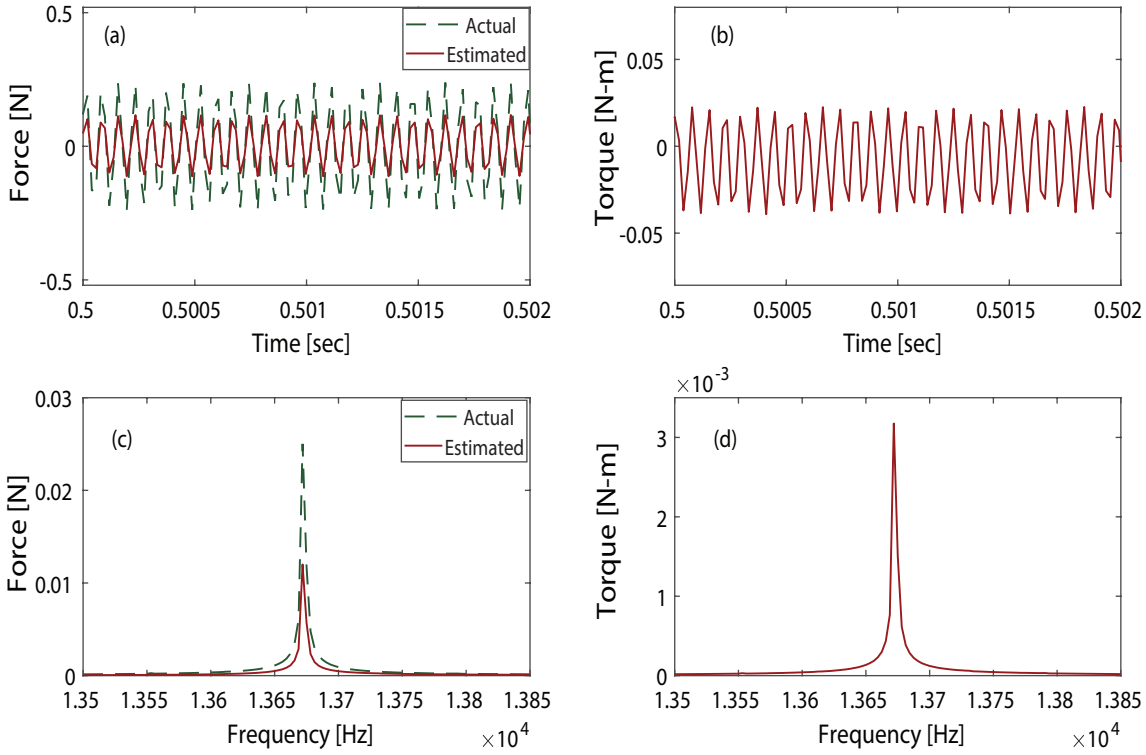

Figure 4.7: (a) Measured and reconstructed forces using Augmented Kalman Filter Method at around 13 kHz. (b) Reconstructed torque using Augmented Kalman Filter Method. (c) FFT of measured and reconstructed forces. (d) FFT of the reconstructed torque. Measured force is shown with dotted line and reconstructed force is shown with solid line.

It can also be deduced that the performance of AKF improves, as the operating frequency of VAD system approaches the 18 kHz mode. The FFT of the actual and estimated forces feature a peak corresponding to the frequency of actuation voltage.

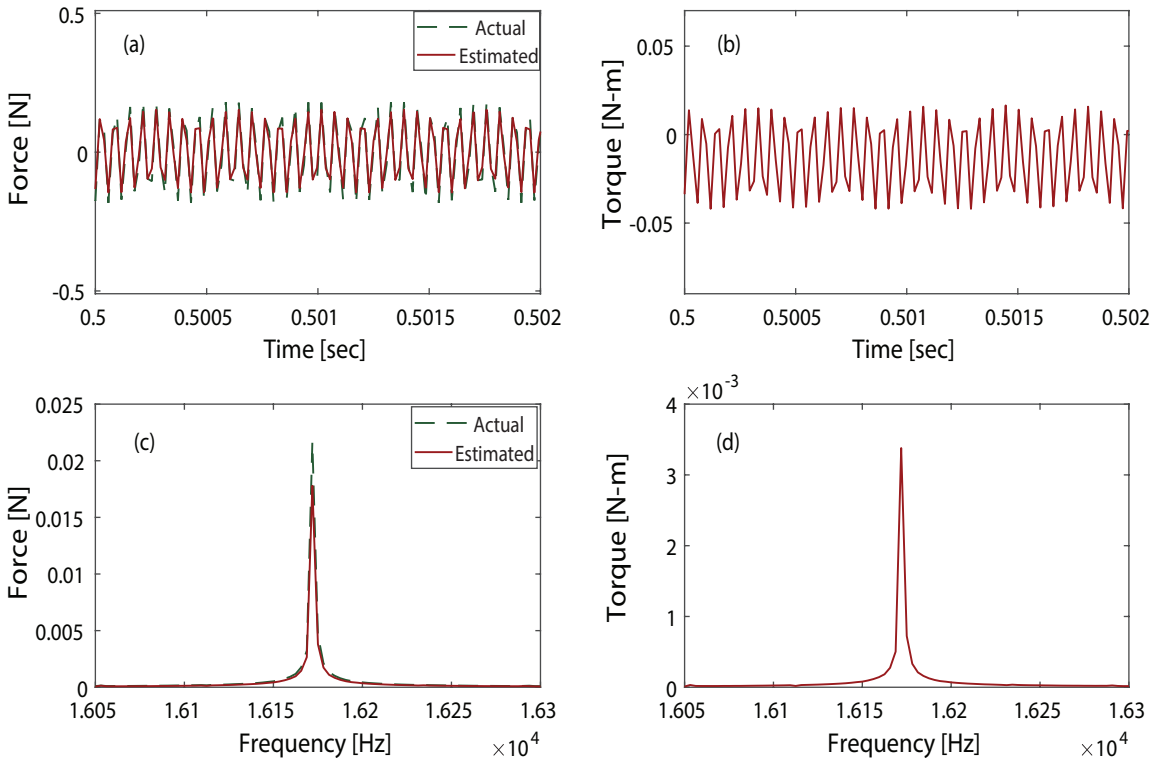

Figure 4.8: (a) Measured and reconstructed forces using Augmented Kalman Filter Method at around 16 kHz. (b) Reconstructed torque using Augmented Kalman Filter Method. (c) FFT of measured and reconstructed forces. (d) FFT of the reconstructed torque. Measured force is shown with dotted line and reconstructed force is shown with solid line.

Finally a very high frequency actuation voltage of around 22 kHz is applied. Reconstructed force and torque are shown in Fig.4.9. Again AKF provides reasonable estimate of measured axial force time history. In this case, a phase lag between the measured and reconstructed axial force is observed. This is due to the low sampling rate (51200 Hz) which is enabling three samples of input and output signals per cycle. So with a very high sampling rate this phase lag may be avoided. Overall it is observed that the forces are reconstructed with good accuracy in a wide range of frequencies.

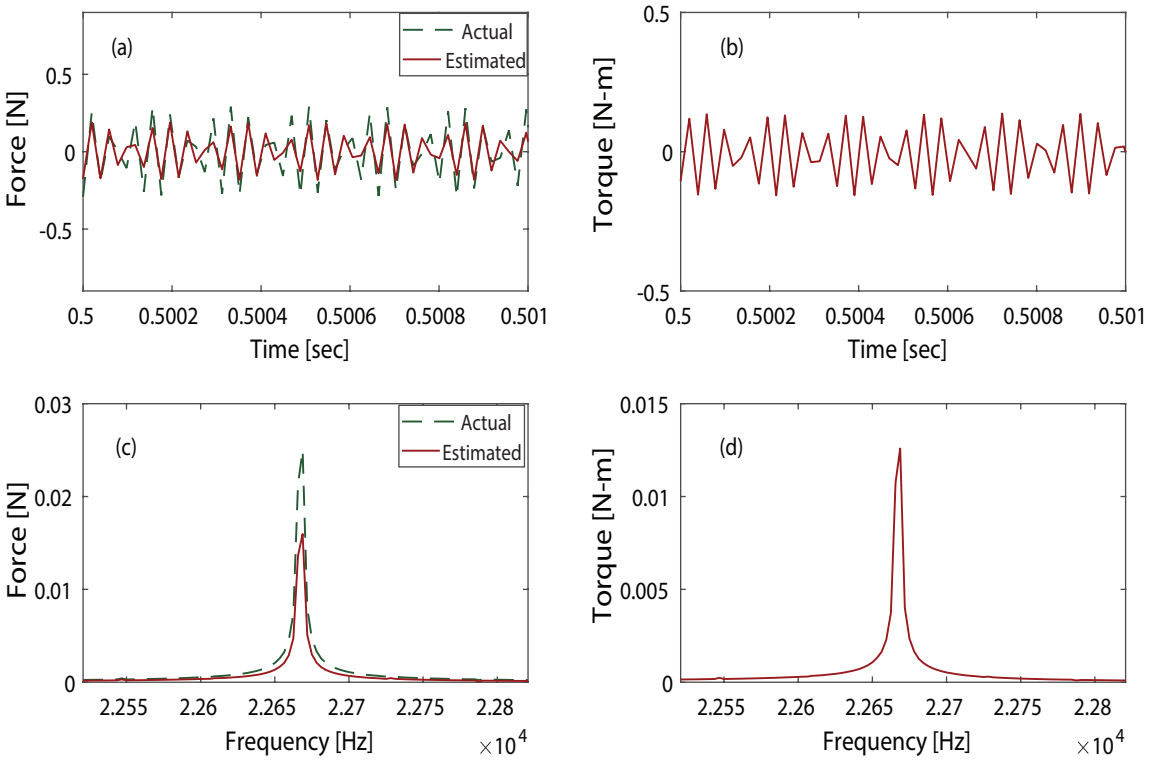

Figure 4.9: (a) Measured and reconstructed forces using Augmented Kalman Filter Method at around 22 kHz. (b) Reconstructed torque using Augmented Kalman Filter Method. (c) FFT of measured and reconstructed forces. (d) FFT of the reconstructed torque. Measured force is shown with dotted line and reconstructed force is shown with solid line.

Chapter 5

Conclusion

In this thesis, thrust force and torque were estimated in a vibration assisted drilling (VAD) system using Augmented Kalman Filter (AKF). The AKF algorithm inversely reconstructed cutting forces from the voltage signal obtained from embedded piezoelectric sensor and torsional deflection from an externally attached accelerometer, while also factoring in the known actuation voltage. For the prediction of two unknown variables, a multi-input multi-output (MIMO) model of the VAD system was constructed from the single-input single-output (SISO) complex FRFs derived utilizing receptance coupling methodology. The complex SISO transfer functions were first transformed into parametric form, with unknown parameters computed using modal parameters obtained from a Matlab tool which is based on two methods: the linear square complex frequency estimator (LSCF) algorithm and least-squares frequency-domain estimator (LSFD) algorithm. Then MIMO transfer function model framework was created using parametric SISO models. Since AKF is implemented on state-space model so it was realized from the MIMO model structure.

Experimental tests were eventually conducted and estimated thrust force results were compared to those measured using a load cell. The filter accurately estimated the input signal of various frequencies and effectively suppressed the dynamic disturbance while simultaneously filtering noise. The estimation analysis was carried out after determining the optimal tuning parameters for force and torque from 3D output estimation and smoothing error norm plots.

5.1 Future work

- **Testing of existing study in actual machining**

  In this study, specifically designed experimental setup was put together to test the feasibility of input signal estimation method. But the proposed method will also need to be validated in an actual machining process, which would necessitate few changes in the toolholder. A microcontroller with circuitry for signal conditioning and wireless transmission of input and output signals will be included in the new modified toolholder. So after the development of wireless signal measurement and transmission setup, the input and output signals may be used in the Augmented Kalman Filter model to estimate cutting forces.

- **Adaptive force control**

  During cutting process, real-time anomalies can be avoided with adaptive control of machining process parameters such as cutting speed and feedrate. In the existing adaptive control solutions, feedrate is adjusted based on preset cutting power, which is measured from spindle motor. However it is more useful to do adaptive control for preset force. So from this work, cutting forces predicted from sensor feedback may be effectively used to execute adaptive force control through the adjustment of process parameters.

- **Machining process monitoring**

  Because of high correlation of cutting forces with real time status of tool and workpiece during machining, they are used as a monitoring signal in machining process monitoring applications. Apart from that cutting forces are also effective in detecting the onset of chatter. Therefore, the estimated cutting forces can be utilized to monitor the dynamic stability of machining process and detect the onset of tool malfunctions, thereby also allowing feedrate or other parameters to be adjusted autonomously.

Appendix A

Additional Information

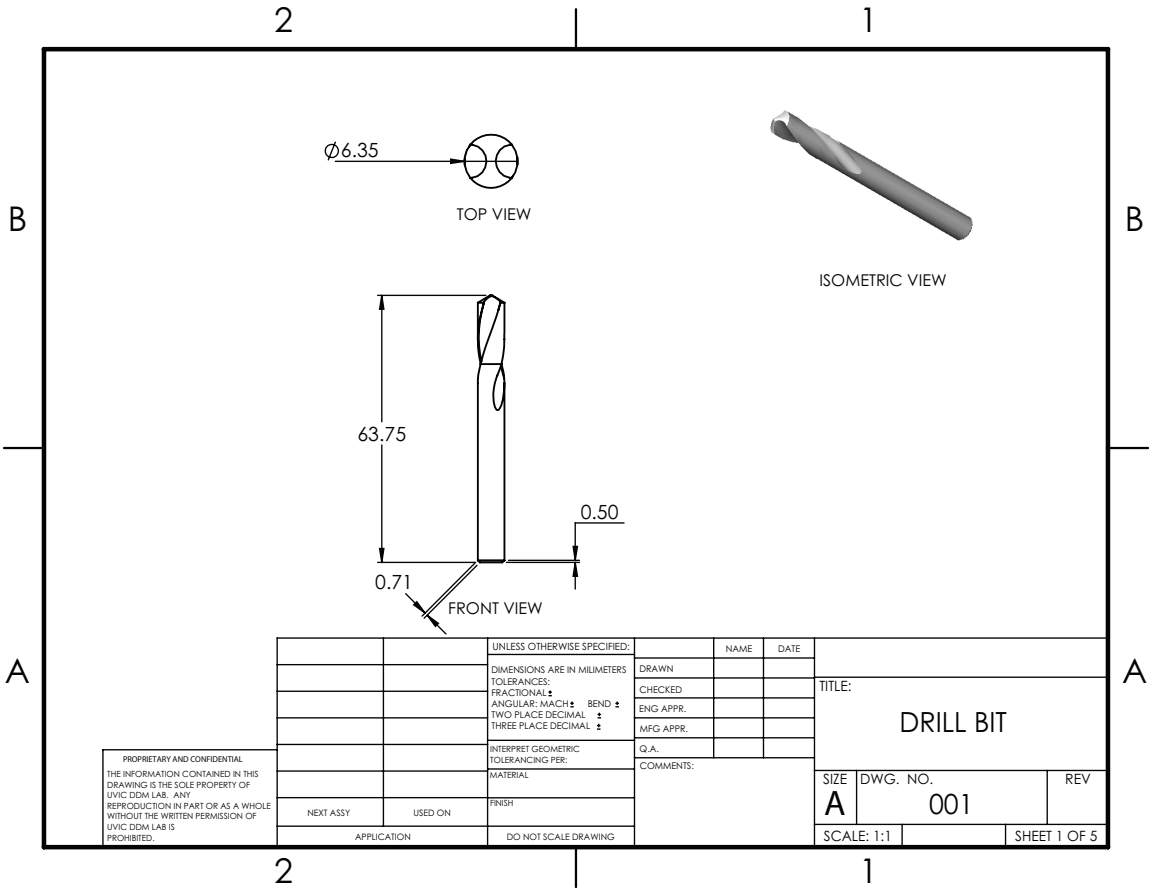

Figure A.1: Drawing of drill bit

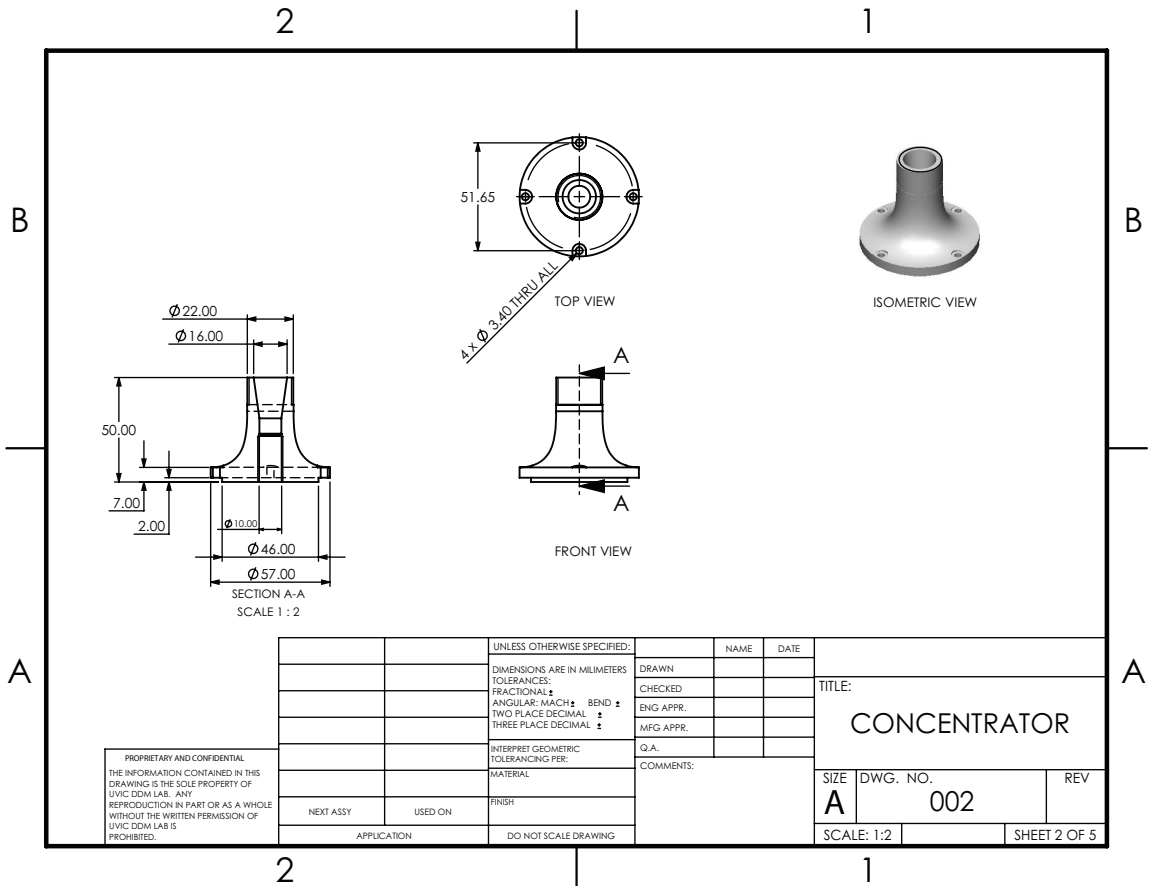

Figure A.2: Drawing of concentrator

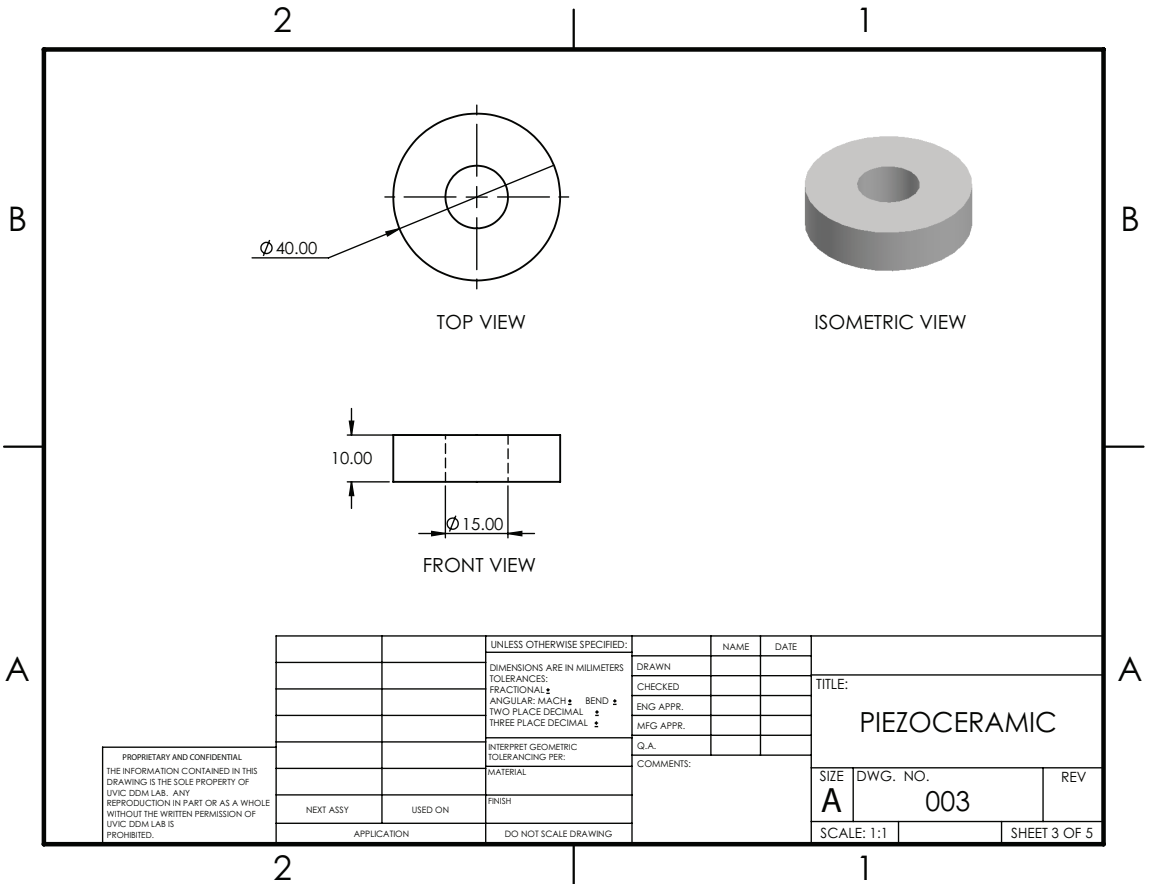

Figure A.3: Drawing of piezoelectric disk

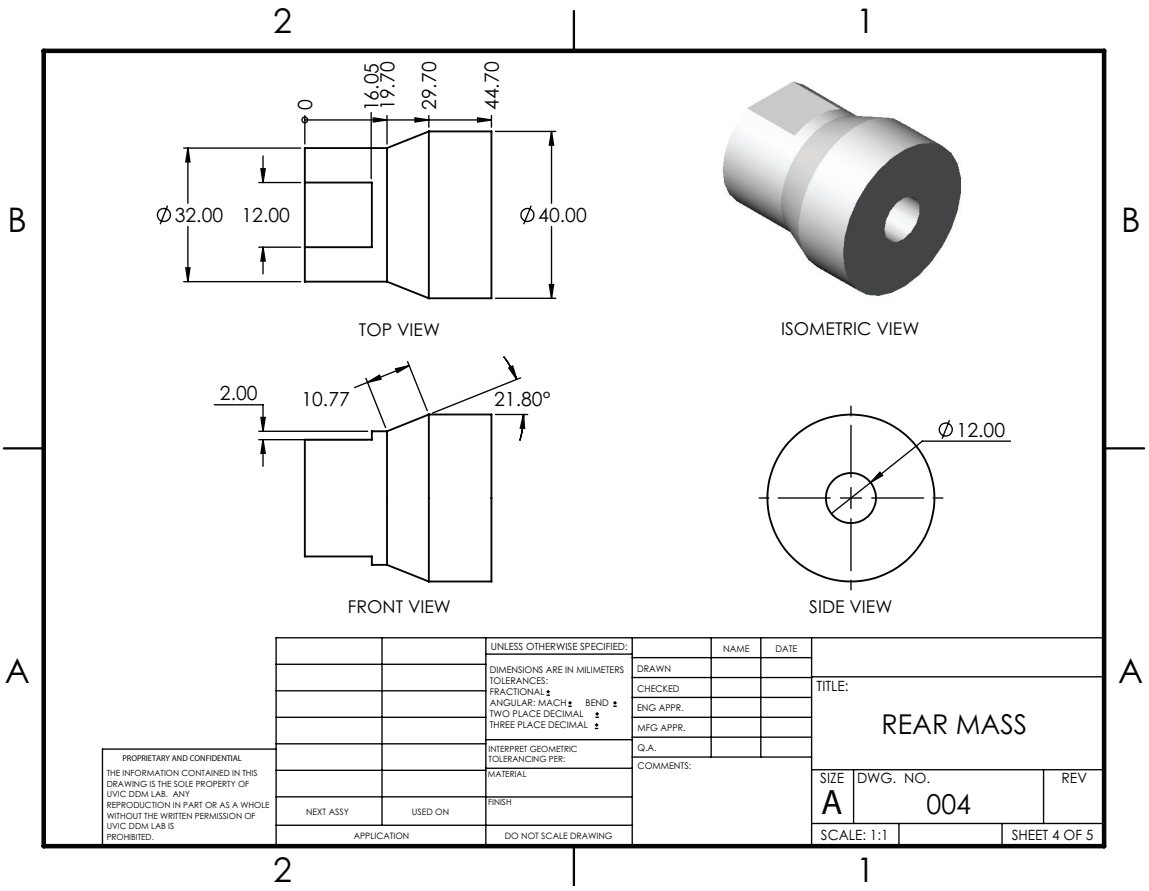

Figure A.4: Drawing of backmass

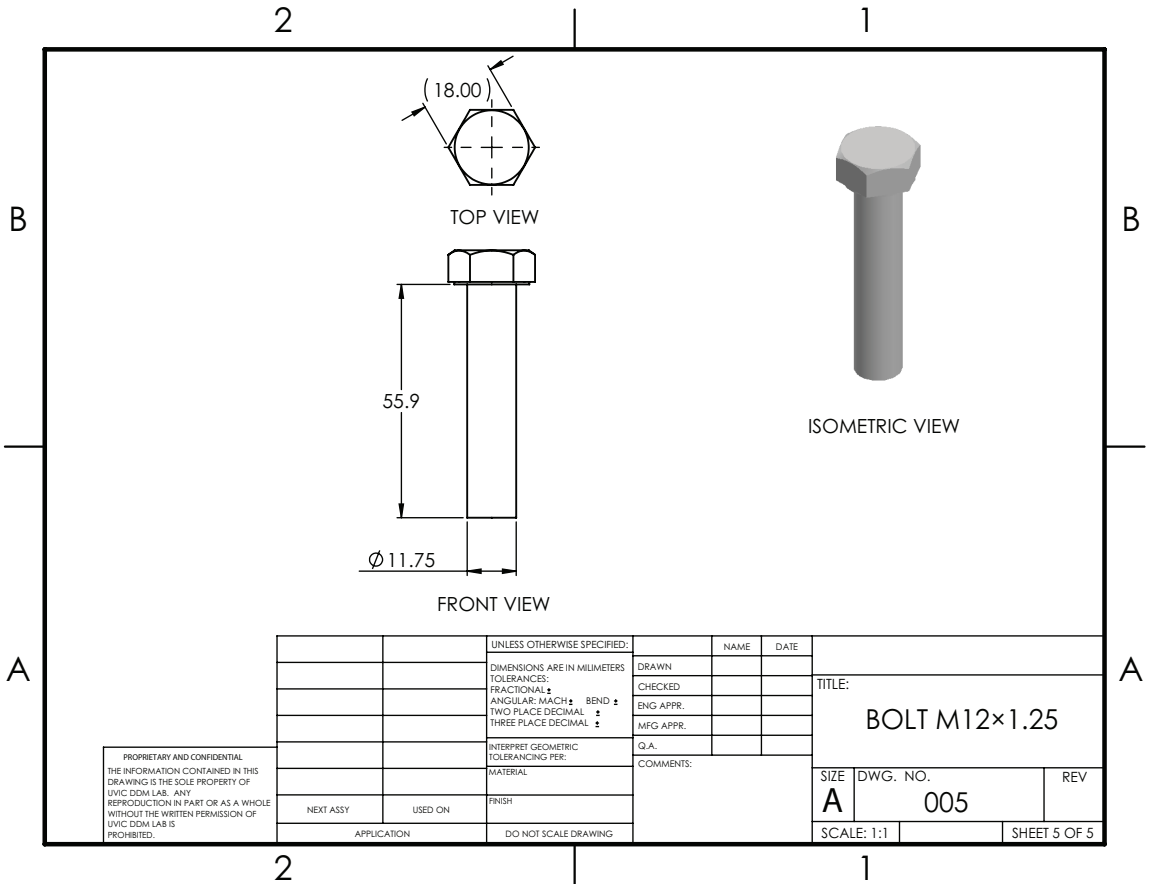

Figure A.5: Drawing of bolt

Bibliography

[1] Paolo Albertelli, Massimo Goletti, Mattia Torta, Mehdi Salehi, and Michele Monno. Model-based broadband estimation of cutting forces and tool vibration in milling through in-process indirect multiple-sensors measurements. *The International Journal of Advanced Manufacturing Technology*, 82(5-8):779–796, 2016.

[2] Deniz Aslan and Yusuf Altintas. Prediction of cutting forces in five-axis milling using feed drive current measurements. *IEEE/ASME Transactions on Mechatronics*, 23(2):833–844, 2018.

[3] Vladimir K Astashev and Vladimir I Babitsky. *Ultrasonic processes and machines: dynamics, control and applications*. Springer Science & Business Media, 2007.

[4] Bahman Azarhoushang and Taghi Tawakoli. Development of a novel ultrasonic unit for grinding of ceramic matrix composites. *The International Journal of Advanced Manufacturing Technology*, 57(9):945–955, 2011.

[5] Robert Grover Brown. *Introduction to random signal analysis and Kalman filtering*. Wiley, 1983.

[6] Baptiste Chomette. Mimo modal parameters identification in frequency domain. *https://www.mathworks.com/matlabcentral/fileexchange/82380-mimo-modal-parameters-identification-in-frequency-domain*, 2022.

[7] Emir Esim and Şahin Yıldırım. Drilling performance analysis of drill column machine using proposed neural networks. *Neural Computing and Applications*, 28(1):79–90, 2017.

[8] David J Ewins. *Modal testing: theory, practice and application*. John Wiley & Sons, 2009.

[9] J Gan, X Wang, M Zhou, B Ngoi, and Z Zhong. Ultraprecision diamond turning of glass with ultrasonic vibration. *The International Journal of Advanced Manufacturing Technology*, 21(12):952–955, 2003.

[10] Kei Harada and Hiroyuki Sasahara. Effect of dynamic response and displacement/stress amplitude on ultrasonic vibration cutting. *Journal of Materials Processing Technology*, 209(9):4490–4495, 2009.

[11] E Jacquelin, A Bennani, and P Hamelin. Force reconstruction: analysis and regularization of a deconvolution problem. *Journal of sound and vibration*, 265(1):81–107, 2003.

[12] Young-Hun Jeong and Dong-Woo Cho. Estimating cutting force from rotating and stationary feed motor currents on a milling machine. *International Journal of Machine Tools and Manufacture*, 42(14):1559–1566, 2002.

[13] Xiaoliang Jin and Narahara Gopal Koya. Investigation of warping effect on coupled torsional-axial vibration of drilling tool. *The International Journal of Advanced Manufacturing Technology*, 86(9):2961–2974, 2016.

[14] A Jullien-Corrigan and K Ahmadi. Measurement of high-frequency milling forces using piezoelectric dynamometers with dynamic compensation. *Precision Engineering*, 66:1–9, 2020.

[15] Rudolph Emil Kalman. A new approach to linear filtering and prediction problems. 1960.

[16] Kistler. Brochure: Cutting force measurements in research and development. *www.kistler.com*, pages 1–52, 2019.

[17] Qiaokang Liang, Dan Zhang, Wanneng Wu, and Kunlin Zou. Methods and research for multi-component cutting force sensing devices and approaches in machining. *Sensors*, 16(11):1926, 2016.

[18] Thierry Miquel. State space modelling. *https://cel.archives-ouvertes.fr/hal-02987750v2*, 2021.

[19] MA Moghaddas, MA Short, NR Wiley, AY Yi, and KF Graff. Improving productivity in an ultrasonic-assisted drilling vertical machining center. *Journal of manufacturing science and engineering*, 140(6), 2018.

[20] Toshimichi Moriwaki, Eiji Shamoto, and Kenji Inoue. Ultraprecision ductile cutting of glass by applying ultrasonic vibration. *CIRP annals*, 41(1):141–144, 1992.

[21] Chandra Nath and M Rahman. Effect of machining parameters in ultrasonic vibration cutting. *International Journal of Machine Tools and Manufacture*, 48(9):965–974, 2008.

[22] Vahid Ostad Ali Akbari. *Modelling the dynamics of vibration assisted drilling systems using substructure analysis*. PhD thesis, 2020.

[23] Vahid Ostad Ali Akbari and Keivan Ahmadi. Substructure analysis of vibration-assisted drilling systems. *The International Journal of Advanced Manufacturing Technology*, 113(9):2833–2848, 2021.

[24] Simon S Park and Yusuf Altintas. Dynamic compensation of spindle integrated force sensors with kalman filter. *J. Dyn. Sys., Meas., Control*, 126(3):443–452, 2004.

[25] Martin Postel, Deniz Aslan, Konrad Wegener, and Yusuf Altintas. Monitoring of vibrations and cutting forces with spindle mounted vibration sensors. *CIRP Annals*, 68(1):413–416, 2019.

[26] SS Rao. Mechanical vibrations fourth edition in si units. *Chapter*, 2:146–148, 2005.

[27] Muhammad Rizal, Jaharah A Ghani, Mohd Zaki Nuawi, and Che Hassan Che Haron. Development and testing of an integrated rotating dynamometer on tool holder for milling process. *Mechanical systems and signal processing*, 52:559–576, 2015.

[28] Muhammad Rizal, Jaharah A Ghani, Mohd Zaki Nuawi, and Che Hassan Che Haron. An embedded multi-sensor system on the rotating dynamometer for real-time condition monitoring in milling. *The International Journal of Advanced Manufacturing Technology*, 95(1):811–823, 2018.

[29] A Rosen. Theoretical and experimental investigation of the nonlinear torsion and extension of initially twisted bars. *ASME J Applied Mechanics*, 50:321–326, 1983.

[30] Zhenyu Shao, Xinggang Jiang, Zhe Li, Daxi Geng, Shaomin Li, and Deyuan Zhang. Feasibility study on ultrasonic-assisted drilling of cfrp/ti stacks by single-shot under dry condition. *The International Journal of Advanced Manufacturing Technology*, 105(1):1259–1273, 2019.

[31] Guoyan Sun, Lingling Zhao, Zhen Ma, and Qingliang Zhao. Force prediction model considering material removal mechanism for axial ultrasonic vibration-assisted peripheral grinding of zerodur. *The International Journal of Advanced Manufacturing Technology*, 98(9):2775–2789, 2018.

[32] K Venkatesan, K Manivannan, S Devendiran, Arun Tom Mathew, Nouby M Ghazaly, SM Neha Benny, et al. Study of forces, surface finish and chip morphology on machining of inconel 825. *Procedia Manufacturing*, 30:611–618, 2019.

[33] Min Wan, Heng Yuan, Jia Feng, Wei-Hong Zhang, and Wei Yin. Industry-oriented method for measuring the cutting forces based on the deflections of tool shank. *International Journal of Mechanical Sciences*, 130:315–323, 2017.

[34] Hui Wang, ZJ Pei, and Weilong Cong. A mechanistic cutting force model based on ductile and brittle fracture material removal modes for edge surface grinding of cfrp composites using rotary ultrasonic machining. *International Journal of Mechanical Sciences*, 176:105551, 2020.

[35] Eser Yarar and Sedat Karabay. Investigation of the effects of ultrasonic assisted drilling on tool wear and optimization of drilling parameters. *CIRP Journal of Manufacturing Science and Technology*, 31:265–280, 2020.

[36] De-yuan Zhang, Xiu-juan Feng, Li-jiang Wang, and Ding-chang Chen. Study on the drill skidding motion in ultrasonic vibration microdrilling. *International journal of machine tools and manufacture*, 34(6):847–857, 1994.

[37] Dongzhe Zhang, Hui Wang, Anthony R Burks, and Weilong Cong. Delamination in rotary ultrasonic machining of cfrp composites: finite element analysis and experimental implementation. *The International Journal of Advanced Manufacturing Technology*, 107(9):3847–3858, 2020.

[38] L-B Zhang, L-J Wang, X-Y Liu, H-W Zhao, X Wang, and H-Y Luo. Mechanical model for predicting thrust and torque in vibration drilling fibre-reinforced composite materials. *International Journal of Machine Tools and Manufacture*, 41(5):641–657, 2001.

[39] Bo Zhao, Wenbo Bie, Xiaobo Wang, Fan Chen, and Baoqi Chang. Design and experimental investigation on longitudinal-torsional composite horn considering the incident angle of ultrasonic wave. *The International Journal of Advanced Manufacturing Technology*, 105(1):325–341, 2019.